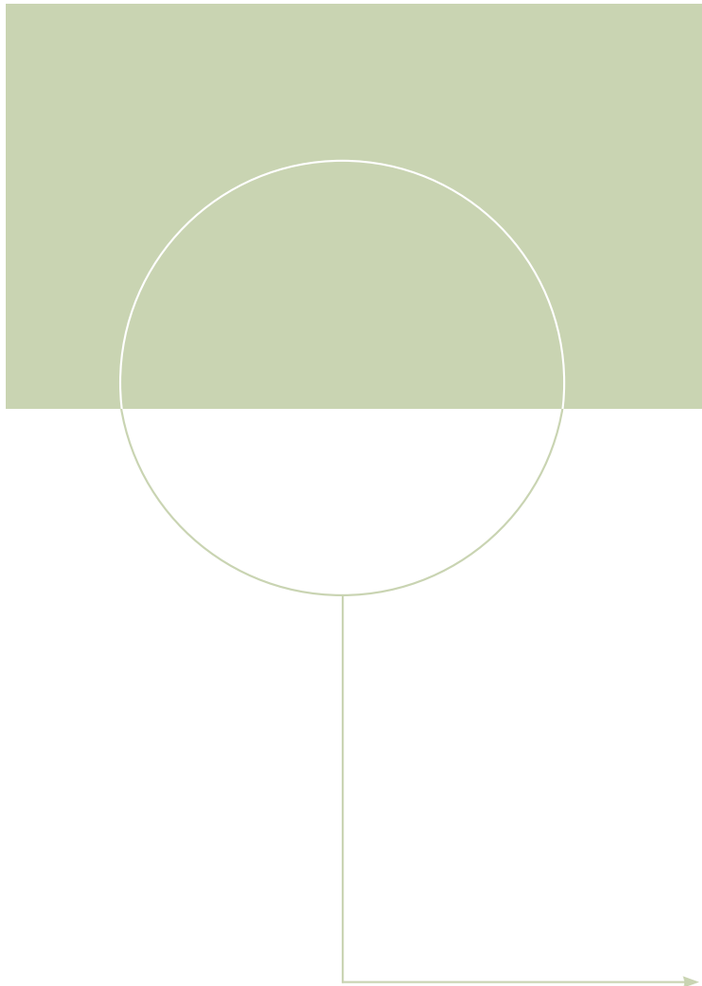

Master's thesis

2019

Muhammad Hamza Khalid

NTNU
Norwegian University of
Science and Technology
Faculty of Information Technology and Electrical
Engineering
Department of Mathematical Sciences

Muhammad Hamza Khalid

Simulating Space-Curved Beams using Structure-Preserving Integration Techniques

June 2019

NTNU
Norwegian University of
Science and Technology

NTNU
Norwegian University of
Science and Technology

NTNU
Norwegian University of
Science and Technology

Simulating Space-Curved Beams using Structure-Preserving Integration Techniques

Muhammad Hamza Khalid

Masters in Mathematical Sciences
Submission date: June 2019
Supervisor: Professor Elena Celledoni
Co-supervisor: Dr. Nikita Kopylov

Norwegian University of Science and Technology
Department of Mathematical Sciences

Abstract

Spatial deformations in beams subjected to terminal twist and axial compression is a significant engineering problem. When compressed more than a limit, the geometry becomes complex and rods form a loop with itself. This unstable behavior is essential to understand post-buckling in rods. The mathematical model used for the analysis of nonlinear deformations is a boundary value problem with a system of ordinary differential equations in space.

In the present work, we use geometric integration schemes to study the deformations in space–curved beams subjected to twist and vertical compression. We present a numerical setup for the solution of boundary value problem and simulate commonly observed phenomena such as loop formation, axial shortening, and self–contact. We also study the conservation properties in space, and numerically compare the preservation performance of structure preserving schemes with non–preserving integration schemes, for a twist–shortening problem. A multi–symplectic formulation for space–curved beams is also derived and numerically implemented using RATTLE and symplectic Euler method. The theoretical and numerical setup presented here will be useful to understand relatively complex dynamic problems.

Preface

This dissertation is submitted to fulfill the requirements for the International Masters in Mathematical Sciences, at the Department of Mathematical Sciences, NTNU. The program code is MSMNFMA.

I want to express gratitude to my supervisor Professor Elena Celledoni, and Dr. Nikita Kopylov for their engagement and guidance throughout the process. I want to dedicate this thesis to my parents, without their love, support and prayers it would never have been possible. In the end, I want to thank my family, and friends for the good time spent in Norway.

Muhammad Hamza Khalid,
June 15, 2019.

Table of Contents

List of Tables

List of Figures

Abbreviations

$\mathbb{R}$	:	Real numbers
$\mathbb{R}^{\mathbf{3}}$	:	3-dimensional vector space of real numbers
$SO(3)$	:	Space of 3×3 orthogonal rotation matrices
$\mathfrak{so}(\mathbf{3})$	:	Lie Algebra whose elements are 3×3 skew-symmetric matrices
S^3	:	3-sphere, $S^3 = \{\mathbb{q} = (q_0, \boldsymbol{q}) \in \mathbb{R} \times \mathbb{R}^3 : q_0^2 + \|\|\boldsymbol{q}\|\|^2 = 1\}$
$\mathfrak{s}^{\mathbf{3}}$	:	Lie algebra of 3-sphere i.e $\mathfrak{s}^3 = T_e S^3 = \{u = (0, \boldsymbol{u}) \in \{0\} \times \mathbb{R}^3 : \boldsymbol{u} \in \mathbb{R}^3\}$
$\frac{d\boldsymbol{u}}{dt}$	:	$\dot{\boldsymbol{u}}$
$\frac{d\boldsymbol{u}}{ds}$	:	$\boldsymbol{u}'$
$\boldsymbol{P}$	:	Stress Resultant
$\boldsymbol{M}$	:	Stress Couple
$\{\gamma_i\}_{i \in \mathcal{I}}$	:	Force Strains
$\{\kappa_i\}_{i \in \mathcal{I}}$	:	Moment Strains
EM	:	Explicit Midpoint Method
IM	:	Implicit Midpoint Method
KM	:	Kahan Method
SM	:	Spherical Midpoint Method
ERK4	:	4th order Runge-Kutta Method
GL4	:	4th order collocation GaussLegendre Method
SE	:	Symplectic Euler Method
RM	:	RATTLE Method

Chapter 1

Introduction

In the present work, we consider a three–dimensional elastic rod model formulated in Reissner (1981). The rod model discusses deformations in space–curved beams and is a static rod model; however, Simo (1985) presents an extension to the generalized dynamic rod model. This model has equal principal stiffness and can experience flexure, torsion, extension, and shear, in contrast to the Kirchhoff–Love model, (Love, 1944) that neglected extension and shear strain. Strain caused due to extension is an important aspect, when investigating the formation of knots and Kirchhoff–Love's model is not feasible to analyze such phenomenon. However, with Reissner (1981) model, it is possible to set up a mathematical model that can experience all four strains. The resulting boundary value formulation can be used for various applications, for instance, twist-shortening problem or a contact problem (Miyazaki and Kondo, 1997). The former is a relatively simplified application, with boundary conditions on the start and end point of the rod, whereas the later has few additional conditions and assumptions which make it a relatively complex problem.

An analytical solution and possible applications for this model were presented in Miyazaki and Kondo (1997); however, the solutions are expressed in integral forms and require appropriate numerical integration techniques. Choice of coordinates for the configuration manifold is a crucial issue for the numerical simulation, and the first numerical discretization of this model presented by Simo and Vu-Quoc (1986) used rotation matrices to represent the configuration manifold. Miyazaki and Kondo (1997) choose Euler angles to represent rotations; however, we have opted to use unit quaternions (Euler parameters). We use the configuration assumptions on the rod from Miyazaki and Kondo (1997) to write the equilibrium equations for space–curved beams in a compact form using vectors. The resulting model is a boundary value problem with a system of ordinary differential equations in space that can be numerically solved using geometric integrators. The problem was investigated for a twist–shortening problem discussed in subsection 2.2.4. Due to the nature of the problem, it is challenging to use integration techniques that preserve geometry, and also satisfy boundary conditions. To overcome this problem, we use the shooting method combined with schemes based on Runge–Kutta methods that treat a boundary

value problem as an initial value problem and uses root finding techniques for the solution. The advantage of the shooting method lies in the usability of time-marching schemes for initial value problems and will be discussed in detail in section 3.1.

One simple approach to the numerical discretization of Hamiltonian PDEs is to semi–discretize them in such a way that the resulting ODE is a Hamiltonian system. This enables the use of symplectic methods or integral preserving methods in time. Another approach is to rewrite the Hamiltonian PDE into a multi–symplectic form (Bridges, 1997) and then provide a space–time discretization of the problem satisfying a discrete local conservation law of multi–symplecticity. As the problem is time–independent, the kinetic energy is zero, and the resulting Hamiltonian formulation has conjugate variables zeros. Therefore it is insignificant to investigate a Hamiltonian formulation. We adopt the work of Celledoni and Säfström (2010), to write the multi–symplectic formulation for Reissner (1981) static model and discuss the conserved quantities in the problem. The simplified formulation presented here will be helpful to understand the multi–symplectic formulations for complex dynamical problems. Ringheim (2013) presented a framework for the multi–symplectic formulation on a static rod model, but no numerical experiments were considered. We do a successful implementation of the multi–symplectic formulation using symplectic integration techniques discussed in chapter 3. The goal of this thesis, therefore, is to numerically simulate deformations in space–curved beams when subjected to torsion and terminal thrust using geometric integration.

The sections below primarily focuses on the definitions of the mathematical terms and gives a brief insight into the requisite concepts for this thesis.

1.1 Lie Group and Lie Algebra

Definition 1.1.1 (Lie Group)**.** An *r-parameter* Lie group is a group G carrying a structure of an r-dimensional smooth manifold, such that the multiplication map $m : G \times G \to G$,

$$m(g, h) = g.h, \qquad g, h \in G,$$

and the inversion map $i : G \to G$,

$$i(g) = g^{-1}, \qquad g \in G,$$

are smooth maps between manifolds (Olver, 2012).

Definition 1.1.2 (Lie Bracket or Commutator)**.** Let $f\colon M \to \mathbb{R}$ be smooth function, and $\boldsymbol{v}$ and $\boldsymbol{w}$ vector fields on M, then their Lie Bracket $[\boldsymbol{v}, \boldsymbol{w}]$ (Olver, 2012) is the unique vector field satisfying

$$[\boldsymbol{v}, \boldsymbol{w}](f) = \boldsymbol{v}(\boldsymbol{w}(f)) - \boldsymbol{w}(\boldsymbol{v}(f)).$$

Proposition 1. *The Lie Bracket has the following properties, (Olver, 2012)*

(a) Bilinearity

$$[c\boldsymbol{v} + c'\boldsymbol{v}', \boldsymbol{w}] = c[\boldsymbol{v}, \boldsymbol{w}] + c'[\boldsymbol{v}', \boldsymbol{w}],$$

where c, c' are constants.

(b) Skew-Symmetry

$$[\boldsymbol{v}, \boldsymbol{w}] = -[\boldsymbol{w}, \boldsymbol{v}],$$

(c) Jacobi Identity

$$[\boldsymbol{u}, [\boldsymbol{v}, \boldsymbol{w}]] + [[\boldsymbol{w}, \boldsymbol{u}], \boldsymbol{v}] + [\boldsymbol{v}, [\boldsymbol{w}, \boldsymbol{u}]] = 0.$$

Definition 1.1.3 (Lie Algebra)**.** A Lie Algebra (Olver, 2012) over a field $\mathbb{K}$ is a vector space $\mathfrak{g}$ with a bilinear map, $[\,,\,]\colon \mathfrak{g} \times \mathfrak{g} \to \mathfrak{g}$, such that the properties mentioned in Proposition 1 are fulfilled, i.e Lie Bracket is bilinear, skew-symmetric and Jacobi Identity is satisfied.

1.2 Multi-Symplectic PDEs

Definition 1.2.1 (Multi-Symplectic PDE)**.** If a PDE can be written in the form of a linear system of ordinary differentiable equations of type,

$$M\boldsymbol{z}_t + K\boldsymbol{z}_s = \nabla_z \mathcal{S}(\boldsymbol{z}), \tag{1.1}$$

where $M \in \mathbb{R}^{d\times d}$ and $K \in \mathbb{R}^{d\times d}$ are skew-symmetric matrices, $z \in \mathbb{R}^d$ and $\mathcal{S} : \mathbb{R}^d \to \mathbb{R}$ is a smooth map, then the PDE is said to be multi-symplectic.

Define two-forms, ω and κ,

$$\omega := \boldsymbol{dz} \wedge M\boldsymbol{dz}, \quad \kappa := \boldsymbol{dz} \wedge K\boldsymbol{dz}, \tag{1.2}$$

such that ω is associated with time direction and defines a symplectic structure on $\mathbb{R}^m$ ($m = \text{rank}M$), whereas κ is associated with space direction and defines a symplectic structure on $\mathbb{R}^k$ ($k = \text{rank}K$) (Bridges and Reich, 2001). Any solution of the variational equation associated with Equation (1.1) satisfies the multi–symplectic conservation law,

$$\partial_t \omega + \partial_s \kappa = 0. \tag{1.3}$$

Another important property associated with Equation (1.1) is the local conservation of energy and momentum, i.e

$$\partial_t e(\boldsymbol{z}) + \partial_s f(\boldsymbol{z}) = 0, \quad \partial_t i(\boldsymbol{z}) + \partial_s g(\boldsymbol{z}) = 0, \tag{1.4}$$

where,

$$e(\boldsymbol{z}) = \mathcal{S}(\boldsymbol{z}) - \frac{1}{2}\boldsymbol{z}_s^T K^T \boldsymbol{z}, \quad f(\boldsymbol{z}) = \frac{1}{2}\boldsymbol{z}_t^T K^T \boldsymbol{z},$$
$$g(\boldsymbol{z}) = \mathcal{S}(\boldsymbol{z}) - \frac{1}{2}\boldsymbol{z}_t^T M^T \boldsymbol{z}, \quad i(\boldsymbol{z}) = \frac{1}{2}\boldsymbol{z}_s^T M^T \boldsymbol{z}.$$

Global conservation quantities for energy $E(\boldsymbol{z})$ and momentum $I(\boldsymbol{z})$ can be obtained by the integration of $f(\boldsymbol{z})$ and $i(\boldsymbol{z})$ over the spatial domain,

$$E(\boldsymbol{z}) = \int_0^L e(\boldsymbol{z})ds, \quad I(\boldsymbol{z}) = \int_0^L i(\boldsymbol{z})ds, \tag{1.5}$$

such that both are conserved, i.e $(d/dt)E(\boldsymbol{z}) = (d/dt)I(\boldsymbol{z}) = 0$.

1.3 First Integrals

Given a differential equation, $\dot{z} = f(z(t))$, the solution traces a curve in $\mathbb{R}^d$ and for a given function $I(z) : \mathbb{R}^d \mapsto \mathbb{R}$ the solution can be evaluated as $I(z(t))$. For some special functions, $I(z(t))$ may be constant along the solutions and such special functions are known as first integrals.

Definition 1.3.1 (First Integral)**.** A non-constant function $I(z)$ is called a *first integral*, if for any solution $z(t)$ of a linear system following holds. (Hairer et al., 2006),

$$I'(z)\ f(z(t)) = 0,\ \Longrightarrow\ I(z(t))\ = \text{Const},$$

They are also known as invariants, and are crucial in geometric integration. The importance of first integrals varies for mechanical systems. They either help in defining the problem, with constant values having physical significance, or help in confining the solution on a bounded region. They also serve as a comparable measure for evaluating the performance of different numerical methods.

For a constant vector d, $I(z) = d^T z$ is called *linear invariant* if $d^T f(z) = 0$ for all z, and for a symmetric $m \times m$ matrix C, $I(z) = z^T C z$ is a *quadratic invariant*.

Theorem 1.3.1. *For a system $\dot{m} = A(m)\ m$, If the matrix A is skew-symmetric for all m, then the quadratic function $I(m) = m^T m$ is an invariant (Marsden and Ratiu, 2013).*

For example, in Equations (1.4) and (1.5) energy and momentum are invariant quantities that are preserved either locally or globally. Global conservation (1.5) is a consequence of local conservation (1.4), therefore, having local conservation is a stronger property. In case of time-independent problems, the conserved quantities hold locally in space (in fact point-wise), hence their integrals over the space domain also remain constant. Their importance for our problem, will be discussed in chapter 2.

1.4 Euler Angles

The orientation of a body in space can be specified using three successive rotations with respect to set of some coordinate axes fixed in the body, provided no two successive axes of the sequence are same. The specific sequence of rotations (Leimkuhler and Reich, 2004, page 228) used by Euler is as follows:

1. Counterclockwise rotation α about the z-axis.
2. Counterclockwise rotation β about the x-axis.
3. Counterclockwise rotation γ about the z-axis.

The rotation matrix $\wedge$ can be expressed using the product of the following three planar rotations, i.e $\wedge = ABC$ where,

$$A = \begin{bmatrix} cos\gamma & sin\gamma & 0 \\ -sin\gamma & cos\gamma & 0 \\ 0 & 0 & 1 \end{bmatrix},\ B = \begin{bmatrix} 1 & 0 & 0 \\ 0 & cos\beta & sin\beta \\ 0 & -sin\beta & cos\beta \end{bmatrix},\ C = \begin{bmatrix} cos\alpha & sin\alpha & 0 \\ -sin\alpha & cos\alpha & 0 \\ 0 & 0 & 1 \end{bmatrix},$$

Elementary rotations A, B, C do not commute, so there are 6 possible conventions for the representation of rotation matrix and the choice of axes for rotations is not unique.

Euler angles used for solving equations of motion of a rigid body do not cover all possible orientations, and singularities in the equations complicate the numerical integration of the resulting equations of motion, not only at the singularity but also in the neighborhood. One way to counter this problem is choosing a different sequence of axes (with new angle variables) whenever integration proceeds in the vicinity of a singular point, but this procedure will make the algorithm cumbersome. Because of this problem with the Euler angle, an alternative set of parameters based on Hamilton's quaternions is often used (Leimkuhler and Reich, 2004).

1.5 Quaternions

A quaternion is quadruple of Euler parameters $\mathbb{q} = (q_0, \boldsymbol{q})$ where q_0 is a scalar and $\boldsymbol{q} = (q_1, q_2, q_3)$ is a vector in three dimensional space. Quaternions (with unit length) are points on the unit three dimensional, S^3 described by the constraint, $\{\mathbb{q} \in \mathbb{R}^4 : ||\mathbb{q}|| = 1\}$. In other words, $\mathbb{q} \in \mathbb{R} \times \mathbb{R}^3$ is equipped with a certain Lie group structure and the product (non–commutative) "$\otimes$" is defined as

$$(p_0, \boldsymbol{p}) \otimes (q_0, \boldsymbol{q}) := (p_0 q_0 - \boldsymbol{p}^T \boldsymbol{q}\,,\; p_0 \boldsymbol{q} + q_0 \boldsymbol{p} + \boldsymbol{p} \times \boldsymbol{q}). \tag{1.6}$$

Product of quaternions can also be expressed as a matrix–vector product, i.e for $\mathbb{p}, \mathbb{q} \in \mathbb{R}^4$, $\mathbb{p} \otimes \mathbb{q} = R(\mathbb{q})\mathbb{p} = L(\mathbb{p})\mathbb{q}$, where $L(\mathbb{p})$ and $R(\mathbb{q})$ are orthogonal commutative matrices defined as

$$L(\mathbb{q}) = \begin{bmatrix} q_0 & -\boldsymbol{q}^T \\ \boldsymbol{q} & (q_0 \mathbb{1} + \hat{\boldsymbol{q}}) \end{bmatrix} \text{ and } R(\mathbb{q}) = \begin{bmatrix} q_0 & -\boldsymbol{q}^T \\ \boldsymbol{q} & (q_0 \mathbb{1} - \hat{\boldsymbol{q}}) \end{bmatrix},$$

where $\mathbb{1} \in \mathbb{R}^3$ is an identity matrix. Their sum is defined as

$$\mathbb{q} + \mathbb{p} = (q_0 + p_0, \boldsymbol{q} + \boldsymbol{p}).$$

For $\mathbb{q} \neq (0, \mathbf{0})$, there exists an inverse, $\mathbb{q}^{-1}$,

$$\mathbb{q}^{-1} = \bar{\mathbb{q}} \,/\, ||\mathbb{q}||, \quad ||\mathbb{q}|| = \sqrt{q_0^2 + ||\boldsymbol{q}||_2^2},$$

where the conjugate of quaternion is $\bar{\mathbb{q}} = (q_0, -\boldsymbol{q})$ and the identity element is $\mathbb{q}_{id} = (1, \mathbf{0})$. A unit quaternion with scalar as zero, i.e $\mathbb{q} = (0, \boldsymbol{q})$, is called a *pure quaternion*. Quaternions are often used to find rotation matrices to avoid dealing with singularities. A unit quaternion $\mathbb{q} = (q_0, \boldsymbol{q})$ can be transformed to rotation matrices using an Euler–Rodrigues map $\mathcal{E} : S^3 \to SO(3)$ defined as

$$\mathcal{E}(\mathbb{q}) = I_3 + 2q_0 \widehat{\boldsymbol{q}} + 2\widehat{\boldsymbol{q}}^2, \tag{1.7}$$

where, "$\widehat{\ }$" is the hat-map.

Definition 1.5.1 (Hat-map)**.** A map $\widehat{\ }: \mathbb{R}^3 \to \mathfrak{so}(3)$ is called hat-map, if for $v \in \mathbb{R}^3$,

$$v = \begin{bmatrix} v_1 \\ v_2 \\ v_3 \end{bmatrix} \to \widehat{v} = \begin{bmatrix} 0 & -v_3 & v_2 \\ v_3 & 0 & -v_1 \\ -v_2 & v_1 & 0 \end{bmatrix},$$

and it satisfies, $\widehat{v}u = v \times u$.

$\mathcal{E}(\mathbb{q})$ is surjective submersion, i.e its differential is surjective everywhere for a differential map between differential manifolds. However, it is not injective as $\mathcal{E}(\mathbb{q}) = \mathcal{E}(-\mathbb{q})$ that implies each rotation matrix will have two pre-images. For this reason, it is insignificant to consider either of one. $\mathcal{E}(\mathbb{q})$ is also a group homomorphism, since $\mathcal{E}(\mathbb{p}\mathbb{q}) = \mathcal{E}(\mathbb{p})\mathcal{E}(\mathbb{q})$. Explicitly writing the Equation (1.7) gives the structure for the rotation matrix

$$\mathcal{E}(\mathbb{q}) = \begin{bmatrix} 1-2(q_2^2+q_3^2) & -2q_0q_3+2q_1q_2 & 2q_0q_2+2q_1q_3 \\ 2q_0q_3+2q_1q_2 & 1-2(q_1^2+q_3^2) & -2q_0q_1+2q_2q_3 \\ -2q_0q_2+2q_1q_3 & 2q_0q_1+2q_2q_3 & 1-2(q_1^2+q_2^2) \end{bmatrix}.$$

Euler parameters are defined in terms of angle-axis parameter. If ϕ is the angle of rotation around the axis $\boldsymbol{k} \in \mathbb{R}^3$ such that, $||\boldsymbol{k}|| = 1$, then $\mathbb{q} = (\cos(\frac{\phi}{2}), \boldsymbol{k}\sin(\frac{\phi}{2}))$ (Schwab, 2002; Coutsias and Romero, 2004; Leimkuhler and Reich, 2004).

It is also possible to obtain Euler–parameters from the rotation matrix. This is done using the method presented by Shepperd (1978). As the map (1.7) is not injective, hence for each rotation matrix there are two possible choices of quaternions. The appropriate choice is decided using criterion such as continuity or $q_0 > 0$. For the ease of evaluation we assume

$$\boldsymbol{z} = \begin{pmatrix} z_0 \\ z_1 \\ z_2 \\ z_3 \end{pmatrix} := 2 \begin{pmatrix} q_0 \\ q_1 \\ q_2 \\ q_3 \end{pmatrix}, \quad \text{and} \quad T := q_{11} + q_{22} + q_{33} = \text{Tr}(\mathcal{E}(\mathbb{q})),$$

where $\{q_{ij}\}_{i,j=1,2,3}$ represents the (i,j) entry of the rotation matrix and $q_{00} := T$. On comparison with Euler–Rodrigues map we can write following symmetric equations for the diagonal entries of $\mathcal{E}(\mathbb{q})$,

$$\begin{aligned} z_0^2 &= 1 + 2q_{00} - T, \quad z_2^2 = 1 + 2q_{22} - T, \\ z_1^2 &= 1 + 2q_{11} - T, \quad z_3^2 = 1 + 2q_{33} - T, \end{aligned} \tag{1.8}$$

Similarly the off–diagonal entries gives the following equations

$$\begin{aligned} z_0z_1 &= q_{32} - q_{23}, \qquad z_2z_3 = q_{32} + q_{23}, \\ z_0z_2 &= q_{13} - q_{31}, \qquad z_3z_1 = q_{13} + q_{31}, \\ z_0z_3 &= q_{21} - q_{12}, \qquad z_1z_2 = q_{21} + q_{12}. \end{aligned} \tag{1.9}$$

The above information can be summarized into the following algorithm, that will be used to find Euler-parameters from a rotation matrix. (Shepperd, 1978; Egeland and Gravdahl, 2002).

Algorithm

1. Compute $p_{ii} := \max\{q_{ii}\}$
2. Compute $|z_i| = \sqrt{1 + 2p_{ii} - T}$
3. Find the sign of z_i using some criteria, like continuity, or $q_0 > 0$.
4. Find remaining z_j from the system of equations (1.8) and (1.9).
5. Compute $\mathbb{q} := (q_0, \boldsymbol{q})$ from $q_i = z_i/2$ for $i \in \mathcal{I}$.

Chapter 2

Space–Curved Beams

To understand a mechanical system that involves deformations in rods, an easy example to start with is a rigid body problem. Rigid body models, such as in Celledoni et al. (2018, 2008); Celledoni and Säfström (2010), were used to investigate applications like offshore pipe-lay operations, free rigid body and molecular dynamics, and they can serve as a good starting point to understand the mechanics of related problems. For convenience, we start with a free rigid body problem. We discuss the possible invariants and their importance and then write the Hamiltonian formulation using unit quaternions. We then write the mathematical model for the equilibrium equations of space–curved beams (Reissner, 1981; Miyazaki and Kondo, 1997) in a compact form using vectorial notation, and discuss the spatially conserved quantities. Using the mathematical model, we derive the multi–symplectic formulation of the rod model and then explain the idea behind twist–shortening. Time derivatives in this thesis will be represented by dot ($\dot{\boldsymbol{u}}$) and spatial derivatives with prime ($\boldsymbol{u}'$).

2.1 Free Rigid Body

2.1.1 Equations of Motion

Consider a rigid body (as shown in Figure 2.1) with center of mass fixed at origin in a convected coordinate system, with $\{n_i(s,\tau)\}_{i\in\mathcal{I}}$ ($\mathcal{I}=\{1,2,3\}$) representing the orthonormal basis of the body frame, and $\{e_i(\tau)\}_{i\in\mathcal{I}}$ the orthonormal basis of a stationary frame. Parameters s and τ stands for space and time respectively. The configuration of the rigid body can then be determined using a rotation matrix $Q\in SO(3)$, which transforms coordinate vectors from stationary frame to the body coordinates, in particular using $n_i = Qe_i$ for $i=1,2,3$. As is conventional, we denote stationary coordinate vectors by lower case letters, whereas body coordinate vectors by upper case letters.

If $\boldsymbol{M}=(M_1,M_2,M_3)$ represents the angular momenta and $I=\text{diag}(I_{xx},I_{yy},I_{zz})$ the inertia tensor in body coordinates, where (I_{xx},I_{yy},I_{zz}) are principal moments of inertia, then in the absence of any external force the equations of motion can be written as

followed:

$$\dot{\boldsymbol{M}} = \widehat{I^{-1}\boldsymbol{M}}\,\boldsymbol{M}, \tag{2.1}$$

$$\dot{Q} = Q\,\widehat{I^{-1}\boldsymbol{M}}. \tag{2.2}$$

Equation (2.1) is written for the angular momenta rather than angular velocity $\boldsymbol{\Omega} = \mathbf{I^{-1}}\boldsymbol{M}$

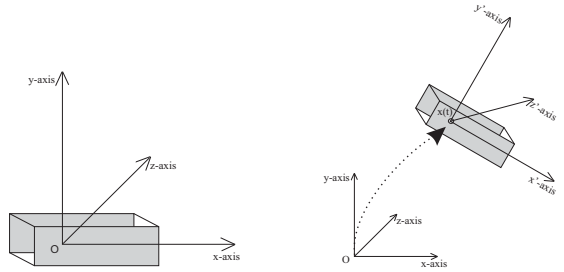

Figure 2.1: Coordinate system representation for a Free Rigid Body

and is known as the Euler equation whereas Equation (2.2) is known as the Arnold equation. (Marsden and Ratiu, 2013; Hairer et al., 2006; Celledoni et al., 2008; Leimkuhler and Reich, 2004) provides more details on rigid bodies. In the next section, we formulate the equations of motion using unit quaternions.

2.1.2 Quaternionic representation of Equations of Motion

In this section, we will write the Equations (2.1) and (2.2) using quaternions, following (Egeland and Gravdahl, 2002). Before finding the quaternionic representation, we will write some helpful results for quaternions. Consider an arbitrary $\mathfrak{q} \in \mathbf{S}^3$. Differentiating $\mathfrak{q} \otimes \bar{\mathfrak{q}} = \mathfrak{q}_{id}$ with respect to t, we get

$$\dot{\mathfrak{q}} \otimes \bar{\mathfrak{q}} + \mathfrak{q} \otimes \dot{\bar{\mathfrak{q}}} = \mathbf{0}, \implies \dot{\bar{\mathfrak{q}}} = -\bar{\mathfrak{q}} \otimes \dot{\mathfrak{q}} \otimes \bar{\mathfrak{q}}. \tag{2.3}$$

Now consider $\dot{\mathfrak{q}} \otimes \bar{\mathfrak{q}}$,

$$\begin{pmatrix} \dot{q_0} \\ \dot{\boldsymbol{q}} \end{pmatrix} \otimes \begin{pmatrix} q_0 \\ -\boldsymbol{q} \end{pmatrix} = \begin{pmatrix} \dot{q_0} q_0 + \dot{\boldsymbol{q}}^T \boldsymbol{q} \\ -\dot{q_0}\boldsymbol{q} + q_0\dot{\boldsymbol{q}} + \boldsymbol{q} \times \dot{\boldsymbol{q}} \end{pmatrix} = \begin{pmatrix} 0 \\ \boldsymbol{v} \end{pmatrix}. \tag{2.4}$$

where $\boldsymbol{v} = -\dot{q_0}\boldsymbol{q} + q_0\dot{\boldsymbol{q}} + \boldsymbol{q} \times \dot{\boldsymbol{q}}$, and we have used the following identity.

$$\frac{1}{2}\frac{d}{dt}(q_0^2 + \boldsymbol{q}^T\boldsymbol{q}) = 0.$$

Now we have gathered the results and we can write a proposition that will give quaternionic representation for Equation (2.2).

Proposition 2. *The quaternionic representation for Equation (2.2) is given by,*

$$\dot{\mathfrak{q}} = \frac{1}{2}\widetilde{\omega} \otimes \mathfrak{q} = \frac{1}{2}\mathfrak{q} \otimes \widetilde{\Omega}, \tag{2.5}$$

where $\widetilde{\omega} = (0,\, \omega)$ and $\widetilde{\Omega} = (0,\, \Omega)$, are unit quaternions representing angular velocity in stationary and body frame, respectively.

Proof. Consider an arbitrary vector $\mathfrak{u} = (0, \boldsymbol{u}) \in \mathfrak{s}^3$ then the coordinate transformation using quaternion product is,

$$\begin{pmatrix} 0 \\ Q\boldsymbol{u} \end{pmatrix} = \mathfrak{q} \otimes \begin{pmatrix} 0 \\ \boldsymbol{u} \end{pmatrix} \otimes \bar{\mathfrak{q}}, \tag{2.6}$$

where $Q \in SO(3)$ is the rotation matrix. Differentiating with respect to time,

$$\begin{aligned}
\begin{pmatrix} 0 \\ \dot{Q}\boldsymbol{u} \end{pmatrix} + \begin{pmatrix} 0 \\ Q\dot{\boldsymbol{u}} \end{pmatrix} &= \dot{\mathfrak{q}} \otimes \begin{pmatrix} 0 \\ \boldsymbol{u} \end{pmatrix} \otimes \bar{\mathfrak{q}} + \mathfrak{q} \otimes \begin{pmatrix} 0 \\ \dot{\boldsymbol{u}} \end{pmatrix} \otimes \bar{\mathfrak{q}} + \mathfrak{q} \otimes \begin{pmatrix} 0 \\ \boldsymbol{u} \end{pmatrix} \otimes \dot{\bar{\mathfrak{q}}}, \\
\begin{pmatrix} 0 \\ \dot{Q}\boldsymbol{u} \end{pmatrix} &= \dot{\mathfrak{q}} \otimes \begin{pmatrix} 0 \\ \boldsymbol{u} \end{pmatrix} \otimes \bar{\mathfrak{q}} + \mathfrak{q} \otimes \begin{pmatrix} 0 \\ \boldsymbol{u} \end{pmatrix} \otimes \dot{\bar{\mathfrak{q}}}, \quad \Big(\text{Using}(2.6) \text{ for } \dot{\boldsymbol{u}}\Big) \\
\begin{pmatrix} 0 \\ \dot{Q}\boldsymbol{u} \end{pmatrix} &= \dot{\mathfrak{q}} \otimes \bar{\mathfrak{q}} \otimes \mathfrak{q} \otimes \begin{pmatrix} 0 \\ \boldsymbol{u} \end{pmatrix} \otimes \bar{\mathfrak{q}} - \mathfrak{q} \otimes \begin{pmatrix} 0 \\ \boldsymbol{u} \end{pmatrix} \otimes \bar{\mathfrak{q}} \otimes \dot{\mathfrak{q}} \otimes \bar{\mathfrak{q}}, \quad \Big(\text{using } (2.3)\Big) \\
\begin{pmatrix} 0 \\ \dot{Q}\boldsymbol{u} \end{pmatrix} &= (\dot{\mathfrak{q}} \otimes \bar{\mathfrak{q}}) \otimes \begin{pmatrix} 0 \\ Q\boldsymbol{u} \end{pmatrix} - \begin{pmatrix} 0 \\ Q\boldsymbol{u} \end{pmatrix} \otimes (\dot{\mathfrak{q}} \otimes \bar{\mathfrak{q}}), \\
\begin{pmatrix} 0 \\ \dot{Q}\boldsymbol{u} \end{pmatrix} &= \begin{pmatrix} 0 \\ \boldsymbol{v} \end{pmatrix} \otimes \begin{pmatrix} 0 \\ Q\boldsymbol{u} \end{pmatrix} - \begin{pmatrix} 0 \\ Q\boldsymbol{u} \end{pmatrix} \otimes \begin{pmatrix} 0 \\ \boldsymbol{v} \end{pmatrix}, \quad \Big(\text{using } (2.4)\Big), \\
\begin{pmatrix} 0 \\ \dot{Q}\boldsymbol{u} \end{pmatrix} &= 2 \begin{pmatrix} 0 \\ \boldsymbol{v} \times Q\boldsymbol{u} \end{pmatrix},
\end{aligned}$$

Comparing it with (2.2) gives, $2\boldsymbol{v} = \omega$. Using this we can write the quaternionic representation as followed

$$\dot{\mathfrak{q}} \otimes \bar{\mathfrak{q}} = \frac{1}{2}\widetilde{\omega}, \implies \dot{\mathfrak{q}} = \frac{1}{2}\widetilde{\omega} \otimes \mathfrak{q}, \tag{2.7}$$

where $\widetilde{\omega} = (0,\, \omega)$. Using (2.7), we can write the following proposition. □

Equation (2.5) can also be written using matrix–vector multiplication as following,

$$\dot{\mathfrak{q}} = \frac{1}{2}R(\mathfrak{q})\widetilde{\omega} = \frac{1}{2}L(\mathfrak{q})\widetilde{\Omega}. \tag{2.8}$$

At each time-step, Equation (2.5) or (2.8) gives quaternion $\mathfrak{q} \in S^3$, and using Euler–Rodrigues map (1.7), we can find the rotation matrix. For a general overview of quaternion representation for kinematics equations see Egeland and Gravdahl (2002); Celledoni et al. (2008); Schwab (2002); Coutsias and Romero (2004).

2.1.3 Quadratic Invariants

The two quadratic invariants for a free rigid body problem are as following, (Hairer et al., 2006; Marsden and Ratiu, 2013)

$$\boldsymbol{M}^T\boldsymbol{M} = M_1^2 + M_2^2 + M_3^2, \tag{2.9}$$

$$H(\boldsymbol{M}) = \frac{1}{2}\langle \boldsymbol{M}, I^{-1}\boldsymbol{M}\rangle = \frac{1}{2}\left(\frac{M_1^2}{I_1} + \frac{M_2^2}{I_2} + \frac{M_3^2}{I_3}\right), \tag{2.10}$$

The first quadratic invariant (2.9) confines the solution to a sphere, whereas the second quadratic invariant (2.10) confines it to the ellipsoid; therefore the solution is constrained to the intersection of sphere and ellipsoid. Preservation of either of these will guarantee the boundedness of solution as $t \to \infty$. These two quadratic invariants will later be used to distinguish the performance of different integrators in chapter 4.

2.1.4 Hamiltonian Formulation

Free rigid body problem can also be solved by writing the problem in terms of canonical coordinates $r = (\mathbb{p}, \mathbb{q})$, using the Hamiltonian formulation. In this section we present a Hamiltonian formulation for the free rigid body problem in unit quaternions, using the idea presented in Maciejewski (1985). For angular velocity $\widetilde{\omega} = (0, \omega) \in \mathfrak{s}^3$, the kinetic energy (2.11) can be written as

$$\mathcal{L} = \frac{1}{2}\langle \omega,\, I\,\omega\rangle = \frac{1}{2}\left(I_1\omega_1^2 + I_2\omega_2^2 + I_3\omega_3^2\right), \tag{2.11}$$

$$\mathcal{L} = \frac{1}{2}\langle\widetilde{\omega}, \widetilde{I}\,\widetilde{\omega}\rangle = \frac{1}{2}\langle\widetilde{\Omega}, \widetilde{I}\,\widetilde{\Omega}\rangle = 2\langle\dot{\mathbb{q}}, L(\mathbb{q})\,\widetilde{I}\,L(\mathbb{q}^c)\dot{\mathbb{q}}\rangle,$$

where

$$\widetilde{I} = \begin{bmatrix}\alpha & \mathbf{0}^T\\ \mathbf{0} & I\end{bmatrix},$$

where $\alpha \neq 0$ is of no physical importance, but is chosen to ensure the regularity of solution. Using Legendre transformation, the expression for the conjugate momenta can be written as,

$$\mathbb{p} = \frac{\partial\mathcal{L}}{\partial\dot{\mathbb{q}}} = 4L(\mathbb{q})\,\widetilde{I}\,L(\mathbb{q}^c)\dot{\mathbb{q}} \implies \dot{\mathbb{q}} = \frac{1}{4}L(\mathbb{q})\,\widetilde{I}^{-1}\,L(\mathbb{q}^c)\mathbb{p}.$$

Therefore, the Hamiltonian formulation for a free rigid body can be written as,

$$\dot{\mathbb{p}} = -\frac{1}{4}L(\mathbb{p})\,\widetilde{I}^{-1}\,L(\mathbb{p}^c)\mathbb{q}, \tag{2.12}$$

$$\dot{\mathbb{q}} = \frac{1}{4}L(\mathbb{q})\,\widetilde{I}^{-1}\,L(\mathbb{q}^c)\mathbb{p}. \tag{2.13}$$

In the next section, we will derive the equilibrium equations for space–curved beams and their multi–symplectic formulation in quaternions, and discuss the important conserved quantities, as we did for the free rigid body.

2.2 Space–Curved Beam

Spatial elastica is the mathematical model used to analyze deformations in space–curved beams. The static rod model under consideration was formulated by Reissner (1981), where the rod can experience flexure, torsion, shear, and extension and has equal principal stiffness. The model, however, was a static problem, and a generalized dynamic problem was later presented by Simo (1985). In this section, we write the equilibrium equations from Miyazaki and Kondo (1997) in a more compact form using vectors and state them as a boundary value problem. We then present a multi–symplectic formulation and discuss the conserved quantities for the model.

2.2.1 Equilibrium Equations in compact form using vectors

Consider a rod of length L, vertically clamped from both ends with the following features, (Miyazaki and Kondo, 1997)

- Equal principle stiffness and uniform cross-section.
- Direct proportionality of stress resultants and stress couples (irrespective of large displacements) on the force and moment strains, respectively.
- No deformations within the cross-section.
- No distributed load along the rod, and only terminal load.

The rod is made of a hyperelastic material, and there are no deformations within the cross-section, therefore its configuration can be fully described by position of its line of centroids by means of map $\boldsymbol{x} : [0, L] \mapsto \mathbb{R}^3$, and the orientation of cross-section at $s \in [0, L]$ (Simo, 1985). Suppose $\{n_i(s, \tau)\}_{i\in\mathcal{I}}$ ($\mathcal{I} = \{1, 2, 3\}$) and $\{e_i(\tau)\}_{i\in\mathcal{I}}$ represents the orthogonal basis vector for the body frame and the stationary frame, respectively where s denotes space and τ time parameter. The origin of the axis is fixed at the centroid of the cross-section, and the equation for the centroid of rod is given by,

$$\boldsymbol{x}' = \gamma_1^b n_1 + \gamma_2^b n_2 + (1 + \gamma_3^b) n_3, \tag{2.14}$$

where $\{\gamma_i^b\}_{i\in\mathcal{I}}$ represents force strains with γ_1^b and γ_2^b measuring shear about n_1 and n_2, while γ_3^b measures extension. For convenience, "b" and "r" in superscript will denote corresponding terms in body frame and stationary frame, respectively. If $\{P_i(s)\}_{i\in\mathcal{I}}$ is the stress resultant and $\{M_i(s)\}_{i\in\mathcal{I}}$ stress couple in body coordinates, then the equilibrium equations can be written as (Reissner, 1981)

$$\begin{aligned}
&P_1' - P_2\kappa_3^b + P_3\kappa_2^b = 0, \quad && M_1' - M_2\kappa_2^b + M_3\kappa_2^b - P_2(1 + \gamma_3^b) + P_3\gamma_2^b = 0,\\
&P_2' - P_3\kappa_1^b + P_1\kappa_3^b = 0, \quad && M_2' - M_3\kappa_1^b + M_1\kappa_3^b - P_3\gamma_1^b + P_1(1 + \gamma_3^b) = 0,\\
&P_3' - P_1\kappa_2^b + P_2\kappa_1^b = 0, && M_3' - M_1\kappa_2^b + M_2\kappa_1^b - P_1\gamma_2^b + P_2\gamma_1^b = 0,
\end{aligned} \tag{2.15}$$

where $\{\kappa_i^b\}_{i\in\mathcal{I}}$ are the moment strains, for torsion and bending. Using the assumption of linear dependence of stress and strain i.e $P_i \propto \gamma_i^b$ and $M_i \propto \kappa_i^b$, expressions for κ^b, γ^b can be calculated.

$$P_1 = K\gamma_1^b,\ P_2 = K\gamma_2^b,\ P_3 = K_3\gamma_3^b,\ \implies \begin{bmatrix}\gamma_1^b\\ \gamma_2^b\\ \gamma_3^b\end{bmatrix} = \begin{bmatrix}\frac{1}{K} & 0 & 0\\ 0 & \frac{1}{K} & 0\\ 0 & 0 & \frac{1}{K_3}\end{bmatrix}\begin{bmatrix}P_1\\ P_2\\ P_3\end{bmatrix}$$
$$M_1 = A\kappa_1^b,\ M_2 = A\kappa_2^b,\ M_3 = A_3\kappa_3^b,\ \implies \begin{bmatrix}\kappa_1^b\\ \kappa_2^b\\ \kappa_3^b\end{bmatrix} = \begin{bmatrix}\frac{1}{A} & 0 & 0\\ 0 & \frac{1}{A} & 0\\ 0 & 0 & \frac{1}{A_3}\end{bmatrix}\begin{bmatrix}M_1\\ M_2\\ M_3\end{bmatrix} \tag{2.16}$$

where A, A_3, K, K_3 are constants representing flexural, torsional, shear, and extensional rigidity respectively. If $\boldsymbol{P} = [P_1, P_2, P_3]^T$ and $\boldsymbol{M} = [M_1, M_2, M_3]^T$, then (2.15) can be written in compact form as

$$\begin{aligned}\boldsymbol{P}' &= -\widehat{C_M^{-1}\boldsymbol{M}}\boldsymbol{P},\\ \boldsymbol{M}' &= -\widehat{C_M^{-1}\boldsymbol{M}}\boldsymbol{M} - \widehat{C_P^{-1}\boldsymbol{P}}\boldsymbol{P} - \widehat{e}_3\boldsymbol{P},\end{aligned} \tag{2.17}$$

where

$$C_M = \text{diag}[A, A, A_3], \quad C_P = \text{diag}[K, K, K_3].$$

Following Simo (1985), we take the derivative of the body frame with respect to space, to find the equation for the rotation matrix.

$$n_i' = k \times n_i, \quad \text{where} \quad k = \kappa_1^b n_1 + \kappa_2^b n_2 + \kappa_3^b n_3 = Q\kappa^b = QC_M^{-1}\boldsymbol{M},$$

where $Q = [n_1, n_2, n_3] \in SO(3)$ is the orthogonal rotation matrix, that will specify the orientation of rod. Similarly, we can write the Equation (2.14) as followed

$$Q' = Q\widehat{C_M^{-1}\boldsymbol{M}}. \tag{2.18}$$

Similarly, the equation for the position vector can be re-written in compact form as follows,

$$\boldsymbol{x}' = QC_P^{-1}\boldsymbol{P} + Qe_3 = QC_P^{-1}\boldsymbol{P} + n_3. \tag{2.19}$$

Combining Equations (2.17), (2.18) and (2.19), results in a boundary value problem that can be used to study deformations in space–curved beams. Now we will discuss the Hamiltonian structure and associated energy for the space–curved beams that will be helpful in the derivation of multi–symplectic formulation in subsection 2.2.3.

Following Simo et al. (1995, 1988), Equations (2.17) can also be calculated by differentiating the free-energy function with respect to the strain measures. If the free-energy is a quadratic function given by the strain measures, then we can write the expression for energy density in space–curved beams as

$$\mathcal{J}(\gamma^r, \kappa^r) := \frac{1}{2}\Big(\langle\gamma^r, D_P\gamma^r\rangle + \langle\kappa^r, D_M\kappa^r\rangle\Big), \tag{2.20}$$

where,

$$D_P = QC_PQ^T, \quad D_M = QC_MQ^T, \quad \gamma^r = \boldsymbol{x}' - Qe_3,$$

and,

$$\gamma^r = Q\gamma^b, \quad \kappa^r = Q\kappa^b, \quad \boldsymbol{p} = Q\boldsymbol{P}, \quad \boldsymbol{m} = Q\boldsymbol{M}. \tag{2.21}$$

Differentiating potential energy (2.20) with respect to γ^r and κ^r, we get

$$\begin{aligned}\boldsymbol{p} &= \frac{\partial}{\partial \gamma^r}\mathcal{J} = D_P\gamma^r \implies \gamma^r = D_P^{-1}\boldsymbol{p},\\ \boldsymbol{m} &= \frac{\partial}{\partial \kappa^r}\mathcal{J} = D_M\kappa^r.\end{aligned}$$

Using (2.21), the above expressions can be written in body coordinates as followed

$$\begin{aligned}\boldsymbol{P} &= Q^T D_P(Q\gamma^b) = C_P\gamma^b, \text{ where } \gamma^b = Q^T\boldsymbol{x}' - e_3,\\ \boldsymbol{M} &= Q^T D_M(Q\kappa^b) = C_M\kappa^b.\end{aligned}$$

The general form for the balance of linear and angular momentum in space are given by (Reissner, 1981)

$$\partial_s \boldsymbol{p} + \widetilde{\boldsymbol{p}} = 0, \tag{2.22}$$

$$\partial_s \boldsymbol{m} + (\partial_s \boldsymbol{x})\times \boldsymbol{p} + \widetilde{\boldsymbol{m}} = 0, \tag{2.23}$$

where $\widetilde{\boldsymbol{p}}$, $\widetilde{\boldsymbol{m}}$, are the external forces and $\boldsymbol{x}$ is the position vector for line of centroid. For derivations of (2.22) and (2.23), see Green and Zerna (1992). The Hamiltonian, i.e the total energy of the system, is given by the sum of kinetic energy and the potential energy, but since the kinetic energy is zero, therefore its Hamiltonian is

$$\mathcal{U} = \frac{1}{2}\int_0^L \langle \gamma^r, D_P\gamma^r\rangle + \langle \kappa^r, D_M\kappa^r\rangle ds. \tag{2.24}$$

Proposition 3. *With no external forces acting on the system equilibrium equations (2.22) and (2.23) gives a system equivalent to system (2.17).*

Proof. Consider Equations (2.22) and (2.23) in body frame with $\widetilde{\boldsymbol{p}} = \widetilde{\boldsymbol{m}} = 0$,

$$\begin{aligned}(2.22) \implies \boldsymbol{p}' &= (Q\boldsymbol{P})' = Q'\boldsymbol{P} + Q\boldsymbol{P}',\\ Q\boldsymbol{P}' &= -Q\widehat{C_M^{-1}\boldsymbol{M}}\boldsymbol{P}, \implies \boldsymbol{P}' = -\widehat{C_M^{-1}\boldsymbol{M}}\boldsymbol{P}.\\ (2.23) \implies \boldsymbol{m}' &= -\boldsymbol{x}'\times\boldsymbol{p},\\ (Q\boldsymbol{M})' &= -(QC_P^{-1}\boldsymbol{P} + Qe_3)\times Q\boldsymbol{P},\\ Q'\boldsymbol{M} + Q\boldsymbol{M}' &= -QC_P^{-1}\boldsymbol{P}\times Q\boldsymbol{P} - Qe_3\times Q\boldsymbol{P},\\ Q\boldsymbol{M}' &= -Q\widehat{C_M^{-1}\boldsymbol{M}}\boldsymbol{M} - (QC_P^{-1}\boldsymbol{P})\times(Q\boldsymbol{P}) - Qe_3\times Q\boldsymbol{P},\\ Q\boldsymbol{M}' &= -Q\widehat{C_M^{-1}\boldsymbol{M}}\boldsymbol{M} + (Q\boldsymbol{P})\times(QC_P^{-1}\boldsymbol{P}) - Qe_3\times Q\boldsymbol{P},\\ \boldsymbol{M}' &= -\widehat{C_M^{-1}\boldsymbol{M}}\boldsymbol{M} + \boldsymbol{P}\times(C_P^{-1}\boldsymbol{P}) - e_3\times\boldsymbol{P},\\ \boldsymbol{M}' &= -\widehat{C_M^{-1}\boldsymbol{M}}\boldsymbol{M} - \widehat{C_P^{-1}\boldsymbol{P}}\boldsymbol{P} - \widehat{e}_3\boldsymbol{P}.\end{aligned}$$

Hence, we conclude that both systems give identical equations. □

2.2.2 Conserved Quantities

As seen in the time–dependent problem, described in subsection 2.1.3, preservation of quadratic first integrals such as energy, momentum, over time is important. Likewise, we consider here scalar functions of solution which are invariant with respect to space variables, i.e the derivative with respect to space s is zero. We refer to them as conserved quantities. The first conserved quantity for the problem, as remarked in Miyazaki and Kondo (1997) is

$$\begin{aligned}
\kappa_1^b P_1 + \kappa_2^b P_2 + \frac{A_3}{A}\kappa_3^b P_3 &= \text{Const}, \\
\frac{1}{A}M_1 P_1 + \frac{1}{A}M_2 P_2 + \frac{A_3}{A_3 A}M_3 P_3 &= \text{Const}, \ \Big(\text{using Equation } (2.16)\Big) \\
\implies \frac{1}{A}(M_1 P_1 + M_2 P_2 + M_3 P_3) &= \text{Const}.
\end{aligned}$$

Similarly, the other conserved quantities are the applied terminal force (defined as the integral of stress resultants over spatial domain) and curvature κ_3. Using compact vector notation the conserved quantities are proved in the propositions below.

Proposition 4. *$\boldsymbol{P}^T\boldsymbol{P}$ and $\boldsymbol{P}^T\boldsymbol{M}$ are the two conserved quantities for the boundary value problem of space–curved beams.*

Proof. Consider the first conserved $\boldsymbol{P}^T\boldsymbol{P}$, and differentiate with respect to s,

$$\begin{aligned}
\boldsymbol{P}'^T\boldsymbol{P} + \boldsymbol{P}^T\boldsymbol{P}' &= (\widehat{-C_M^{-1}\boldsymbol{M}\boldsymbol{P}})^T\boldsymbol{P} + \boldsymbol{P}^T(\widehat{-C_M^{-1}\boldsymbol{M}\boldsymbol{P}}), \\
&= (\boldsymbol{P}\times C_M^{-1}\boldsymbol{M})^T\boldsymbol{P} + \boldsymbol{P}^T(\boldsymbol{P}\times C_M^{-1}\boldsymbol{M}).
\end{aligned}$$

Using property of scalar triple product $\boldsymbol{u}^T(\boldsymbol{v}\times\boldsymbol{w}) = \boldsymbol{v}^T(\boldsymbol{w}\times\boldsymbol{u}) = \boldsymbol{w}^T(\boldsymbol{u}\times\boldsymbol{v})$ and commutative property $\boldsymbol{u}^T\boldsymbol{v} = \boldsymbol{v}^T\boldsymbol{u}$,

$$\begin{aligned}
\boldsymbol{P}'^T\boldsymbol{P} + \boldsymbol{P}^T\boldsymbol{P}' &= C_M^{-1}\boldsymbol{M}(\boldsymbol{P}\times\boldsymbol{P}) + C_M^{-1}\boldsymbol{M}(\boldsymbol{P}\times\boldsymbol{P}) = 0, \\
\implies \boldsymbol{P}^T\boldsymbol{P} &= \text{Const}.
\end{aligned}$$

Now, consider the second conserved quantity, $\boldsymbol{P}^T\boldsymbol{M}$ and differentiate again with respect to s

$$\begin{aligned}
\boldsymbol{P}'^T\boldsymbol{M} + \boldsymbol{P}^T\boldsymbol{M}' &= (\widehat{-C_M^{-1}\boldsymbol{M}\boldsymbol{P}})^T\boldsymbol{M} + \boldsymbol{P}^T(\widehat{-C_M^{-1}\boldsymbol{M}\boldsymbol{M}} - \widehat{C_P^{-1}\boldsymbol{P}\boldsymbol{P}} - \widehat{\mathbf{e_3}\boldsymbol{P}}), \\
&= (\boldsymbol{P}\times C_M^{-1}\boldsymbol{M})^T\boldsymbol{M} + \boldsymbol{P}^T(\boldsymbol{M}\times C_M^{-1}\boldsymbol{M} + \boldsymbol{P}\times C_P^{-1}\boldsymbol{P} - \mathbf{e_3}\times\boldsymbol{P}), \\
&= (\boldsymbol{P}\times C_M^{-1}\boldsymbol{M})^T\boldsymbol{M} + \boldsymbol{P}^T(\boldsymbol{M}\times C_M^{-1}\boldsymbol{M}) + \underbrace{\boldsymbol{P}^T(\boldsymbol{P}\times C_P^{-1}\boldsymbol{P})}_{=0} - \underbrace{\boldsymbol{P}^T(\mathbf{e_3}\times\boldsymbol{P})}_{=0}, \\
&= \boldsymbol{M}^T(\boldsymbol{P}\times C_M^{-1}\boldsymbol{M}) + \boldsymbol{P}^T(\boldsymbol{M}\times C_M^{-1}\boldsymbol{M}),
\end{aligned}$$

Using property of scalar triple product we can write, $\boldsymbol{M}^T(\boldsymbol{P}\times C_M^{-1}\boldsymbol{M}) = -\boldsymbol{P}^T(\boldsymbol{M}\times C_M^{-1}\boldsymbol{M})$,

$$\begin{aligned}
\boldsymbol{P}'^T\boldsymbol{M} + \boldsymbol{P}^T\boldsymbol{M}' &= -\boldsymbol{P}^T(\boldsymbol{M}\times C_M^{-1}\boldsymbol{M}) + \boldsymbol{P}^T(\boldsymbol{M}\times C_M^{-1}\boldsymbol{M}) = 0, \\
\implies \boldsymbol{P}^T\boldsymbol{M} &= \text{Const}.
\end{aligned}$$

□

To verify local the conservation of energy (1.4) over the spatial domain, we re-write equations (2.17) in the form $\boldsymbol{y}' = B(\boldsymbol{y})\nabla_{\boldsymbol{y}}\mathcal{J}(\boldsymbol{y})$,

$$\begin{pmatrix} \boldsymbol{P}' \\ \boldsymbol{M}' \end{pmatrix} = \begin{pmatrix} \boldsymbol{0} & \hat{\boldsymbol{P}} \\ \hat{\boldsymbol{P}} & \hat{\boldsymbol{M}} \end{pmatrix} \begin{pmatrix} C_P^{-1}\boldsymbol{P} + e_3 \\ C_M^{-1}\boldsymbol{M} \end{pmatrix}, \tag{2.25}$$

where $B(\boldsymbol{y})$ is a skew-symmetric matrix and $\mathcal{J}(\boldsymbol{y})$ energy (2.20) in body coordinates. i.e,

$$\mathcal{J} = \frac{1}{2}\langle \boldsymbol{P}, C_P^{-1}\boldsymbol{P} + 2e_3\rangle + \frac{1}{2}\langle \boldsymbol{M}, C_M^{-1}\boldsymbol{M}\rangle. \tag{2.26}$$

Proposition 5. *Energy density (2.26) is constant over the spatial domain.*

Proof. Differentiating Equation (2.26) with respect to space "s".

$$\begin{aligned}
\mathcal{J}'(\boldsymbol{y}) &= (C_P^{-1}\boldsymbol{P})^T\boldsymbol{P}' + e_3^T\boldsymbol{P}' + (C_M^{-1}\boldsymbol{M})^T\boldsymbol{M}', \\
&= (C_P^{-1}\boldsymbol{P})^T(\boldsymbol{P}\times C_M^{-1}\boldsymbol{M}) + e_3^T(\boldsymbol{P}\times C_M^{-1}\boldsymbol{M}) \\
&\qquad + (C_M^{-1}\boldsymbol{M})^T(\boldsymbol{M}\times C_M^{-1}\boldsymbol{M} + \boldsymbol{P}\times C_P^{-1}\boldsymbol{P} + \boldsymbol{P}\times e_3), \\
&= (C_P^{-1}\boldsymbol{P})^T(\boldsymbol{P}\times C_M^{-1}\boldsymbol{M}) + e_3^T(\boldsymbol{P}\times C_M^{-1}\boldsymbol{M}) \\
&\qquad + (C_M^{-1}\boldsymbol{M})^T(\boldsymbol{P}\times C_P^{-1}\boldsymbol{P}) + (C_M^{-1}\boldsymbol{M})^T(\boldsymbol{P}\times e_3), \\
&= -(C_M^{-1}\boldsymbol{M})^T(\boldsymbol{P}\times C_P^{-1}\boldsymbol{P}) + e_3^T(\boldsymbol{P}\times C_M^{-1}\boldsymbol{M}) \\
&\qquad + (C_M^{-1}\boldsymbol{M})^T(\boldsymbol{P}\times C_P^{-1}\boldsymbol{P}) - e_3^T(\boldsymbol{P}\times C_M^{-1}\boldsymbol{M}), \\
&= 0.
\end{aligned}$$

From $\mathcal{J}'(\boldsymbol{y}) = 0$, we conclude (2.26) is constant over spatial domain. □

The idea of conservation of energy is followed from local conservation laws (1.4) and (1.5) for multi–symplectic PDEs discussed in section 1.2. However, since the problem is time–independent, the energy density differentiated with respect to time in (1.4) disappears. We are then left with a derivative of energy density due to strain, i.e $\mathcal{J}$ with respect to s, and in Proposition 5 we have shown it is equal to zero, therefore we say energy is locally (in fact point-wise) conserved. Since having local conservation is a stronger property and global conservation is its consequence, therefore we say $\mathcal{J}$ is conserved globally as well, i.e (1.5) is satisfied.

2.2.3 Multi–Symplectic Formulation

Using the idea presented in subsection 2.1.2, the equilibrium equation (2.18) for the position matrix can also be written in unit quaternions as followed

$$\mathfrak{q}' = \mathfrak{q}\otimes\widetilde{\kappa}^r = \widetilde{\kappa}^b\otimes\mathfrak{q},$$

for $\widetilde{\kappa}^r = (0,\kappa^r) \in \mathfrak{s}^3$ and $\widetilde{\kappa}^b = (0,\kappa^b) \in \mathfrak{s}^3$. Or using matrix–vector multiplication,

$$\mathfrak{q}' = \frac{1}{2}L(\mathfrak{q})\widetilde{\kappa}^b = \frac{1}{2}R(\mathfrak{q})\widetilde{\kappa}^r.$$

Similarly, Equation (2.19) in unit quaternions is as followed

$$\boldsymbol{x}' = \mathcal{E}(\mathbb{q})\, C_P^{-1}\boldsymbol{P} + n_3,$$

where $\mathcal{E}(\mathbb{q})$ is the rotation matrix calculated using Euler–Rodrigues map (1.7). As discussed in chapter 1, it is insignificant to consider Hamiltonian formulation, because of zero conjugate variables. We therefore derive a multi–symplectic formulation for space–curved beams, that will be applied to twist–shortening problem in chapter 4.

Following Celledoni and Säfström (2010), consider a smooth map $\mathcal{S}$ defined on $\boldsymbol{u} = (\boldsymbol{x}, \mathbb{q})$ for conjugate variables $\boldsymbol{v} = (\boldsymbol{v_x}, \mathbb{v})$ defined as

$$\mathcal{S}(\boldsymbol{u}, \boldsymbol{v}) := \langle \boldsymbol{v}, \boldsymbol{u}_s(\boldsymbol{v})\rangle - \mathcal{L}(\boldsymbol{u}, \boldsymbol{u}_s), \tag{2.27}$$

where $\mathcal{L}$ is the Lagrangian. For convenience, $C_M \in \mathbb{R}^{3\times 3}$ is extended to invertible $\widetilde{C}_M \in \mathbb{R}^{4\times 4}$ so that the new Lagrangian becomes regular on the cotangent bundle.

$$\widetilde{D}_M = L(\mathbb{q})R(\mathbb{q}^c)\widetilde{C}_M L(\mathbb{q}^c)R(\mathbb{q}), \text{ where } \widetilde{C}_M = \begin{bmatrix}\alpha & \mathbf{0}^T \\ \mathbf{0} & C_M\end{bmatrix},\ \alpha \neq 0.$$

The Lagrangian in general is given by the difference of the potential energy and the kinetic energy, but since the kinetic energy is zero, we can use the potential energy (2.20) to write the Lagrangian in quaternions with a holonomic constraint $g(\mathbb{q}) := ||\mathbb{q}||^2 - 1 = 0$.

$$\mathcal{L}(\boldsymbol{u}, \boldsymbol{u}_s) = -\frac{1}{2}\Big[\langle \gamma^r, D_P\gamma^r\rangle + 4\langle \mathbb{q}', R(\mathbb{q})\widetilde{D}_M R(\mathbb{q}^c)\mathbb{q}'\rangle\Big] - \lambda\Big(||\mathbb{q}||^2 - 1\Big), \tag{2.28}$$

where $\gamma^r = \boldsymbol{x}' - n_3$. Analogous to the canonical system written for a free rigid body, we can write a similar system for conjugate variables by taking partial derivatives of the Lagrangian with respect to the space derivatives

$$\boldsymbol{v_x} := \frac{\partial \mathcal{L}}{\partial \boldsymbol{x}'} = -D_P\gamma^r,\ \Longrightarrow\ \boldsymbol{x}'(\mathbb{q}, \boldsymbol{v_x}) = -D_P^{-1}\boldsymbol{v_x} + \epsilon(\mathbb{q})e_3, \tag{2.29}$$

$$\mathbb{v} := \frac{\partial \mathcal{L}}{\partial \mathbb{q}'} = -4R(\mathbb{q})\widetilde{D}_M R(\mathbb{q}^c)\mathbb{q}' \in T^*S^3,\ \Longrightarrow\ \mathbb{q}'(\mathbb{q}, \mathbb{v}) = -\frac{1}{4}R(\mathbb{q})\widetilde{D}_M^{-1}R(\mathbb{q}^c)\mathbb{v}, \tag{2.30}$$

Using these conjugate variables, we rewrite the Equations (2.28) and (2.27),

$$\begin{aligned}
(2.28)\ \Longrightarrow\ \mathcal{L}(\boldsymbol{u}, \boldsymbol{u}_s) &= -\frac{1}{2}\Big[\langle \gamma^r, D_P\gamma^r\rangle + 4\langle \mathbb{q}', R(\mathbb{q})\widetilde{D}_M R(\mathbb{q}^c)\mathbb{q}'\rangle\Big] - \lambda\Big(||\mathbb{q}||^2 - 1\Big), \\
\mathcal{L}(\boldsymbol{u}, \boldsymbol{u}_s) &= -\frac{1}{2}\Big[\langle -D_P^{-1}\boldsymbol{v_x}, D_P(-D_P^{-1}\boldsymbol{v_x})\rangle + \frac{1}{4}\langle \mathbb{v}, R(\mathbb{q})\widetilde{D}_M^{-1}R(\mathbb{q}^c)\mathbb{v}\rangle\Big] \\
&\qquad - \lambda\Big(||\mathbb{q}||^2 - 1\Big), \\
\mathcal{L}(\boldsymbol{u}, \boldsymbol{u}_s) &= -\frac{1}{2}\Big[\langle \boldsymbol{v_x}, D_P^{-1}\boldsymbol{v_x}\rangle + \frac{1}{4}\langle \mathbb{v}, R(\mathbb{q})\widetilde{D}_M^{-1}R(\mathbb{q}^c)\mathbb{v}\rangle\Big] - \lambda\Big(||\mathbb{q}||^2 - 1\Big).
\end{aligned}$$

Calculating $\langle \boldsymbol{v}, \boldsymbol{u}_s(\boldsymbol{v})\rangle$ in (2.27),

$$\begin{aligned}
\langle \boldsymbol{v}, \boldsymbol{u}_s(\boldsymbol{v})\rangle &= \langle \boldsymbol{v_x}, \boldsymbol{x}'\rangle + \langle \mathbb{v}, \mathbb{q}'\rangle, \\
&= \langle \boldsymbol{v_x}, -D_P^{-1}\boldsymbol{v_x} + \epsilon(\mathbb{q})e_3\rangle + \frac{1}{4}\langle \mathbb{v}, R(\mathbb{q})\widetilde{D}_M^{-1}R(\mathbb{q}^c)\mathbb{v}\rangle, \\
&= -\langle \boldsymbol{v_x}, D_P^{-1}\boldsymbol{v_x} - \epsilon(\mathbb{q})e_3\rangle + \frac{1}{4}\langle \mathbb{v}, R(\mathbb{q})\widetilde{D}_M^{-1}R(\mathbb{q}^c)\mathbb{v}\rangle.
\end{aligned}$$

$$
\begin{aligned}
(2.27) \implies \mathcal{S}(\boldsymbol{u},\boldsymbol{v}) &= \langle \boldsymbol{v}, \boldsymbol{u}_s(\boldsymbol{v})\rangle - \mathcal{L}(\boldsymbol{u},\boldsymbol{u}_s),\\
&= -\langle \boldsymbol{v_x}, D_P^{-1}\boldsymbol{v_x} - \epsilon(\mathbb{q})e_3\rangle + \frac{1}{4}\langle \mathbb{v}, R(\mathbb{q})\widetilde{D}_M^{-1}R(\mathbb{q}^c)\mathbb{v}\rangle\\
&\quad + \frac{1}{2}\Big[\langle \boldsymbol{v_x}, D_P^{-1}\boldsymbol{v_x})\rangle + \frac{1}{4}\langle \mathbb{v}, R(\mathbb{q})\widetilde{D}_M^{-1}R(\mathbb{q}^c)\mathbb{v}\rangle\Big]\\
&\qquad + \lambda\Big(||\mathbb{q}||^2 - 1\Big),\\
&= -\frac{1}{2}\Big[\langle \boldsymbol{v_x}, D_P^{-1}\boldsymbol{v_x} - 2\epsilon(\mathbb{q})e_3\rangle + \frac{1}{4}\langle \mathbb{v}, R(\mathbb{q})\widetilde{D}_M^{-1}R(\mathbb{q}^c)\mathbb{v}\rangle\Big]\\
&\qquad + \lambda\Big(||\mathbb{q}||^2 - 1\Big).
\end{aligned}
$$

Summarizing (2.27) as

$$
\mathcal{S}(\boldsymbol{u},\boldsymbol{v}) = -\frac{1}{2}\Big[\langle \boldsymbol{v_x}, D_P^{-1}\boldsymbol{v_x} - 2\epsilon(\mathbb{q})e_3\rangle + \frac{1}{4}\langle \mathbb{v}, R(\mathbb{q})\widetilde{D}_M^{-1}R(\mathbb{q}^c)\mathbb{v}\rangle\Big] + \lambda\Big(||\mathbb{q}||^2 - 1\Big). \tag{2.31}
$$

The partial derivatives of $\mathcal{S}$ with respect to $\boldsymbol{x}$ and $\mathbb{q}$ are given as

$$
\frac{\partial S}{\partial \boldsymbol{x}} = 0, \tag{2.32}
$$

and

$$
\begin{aligned}
\frac{\partial S}{\partial \mathbb{q}} = \frac{1}{4}R(\mathbb{q})L(\mathbb{v})L(\mathbb{q}^c)\widetilde{D}_M^{-1}R(\mathbb{q}^c)\mathbb{v} + R(\mathbb{q})\left[L(\boldsymbol{v_x}) - R(\boldsymbol{v_x})\right]\begin{bmatrix}0\\ D_P^{-1}\boldsymbol{v_x} - \epsilon(\mathbb{q})e_3\end{bmatrix}\\
+ 2\langle(\epsilon(\mathbb{q}) - \mathbb{1})\boldsymbol{v_x}, D_P^{-1}\boldsymbol{v_x} - \epsilon(\mathbb{q})e_3\rangle + 2\lambda\mathbb{q}.
\end{aligned} \tag{2.33}
$$

We can then write equations for the multi–symplectic system (1.1) as follows (Celledoni and Säfström, 2010):

$$
\frac{\partial \mathcal{S}}{\partial \boldsymbol{u}} = -\partial_s \boldsymbol{v}, \tag{2.34}
$$

$$
\frac{\partial \mathcal{S}}{\partial \boldsymbol{v}} = \partial_s \boldsymbol{u}, \tag{2.35}
$$

$$
0 = ||\mathbb{q}||^2 - 1, \tag{2.36}
$$

Or in matrix–vector notation,

$$
\begin{bmatrix}0 & -\mathbb{1} & 0\\ \mathbb{1} & 0 & 0\\ 0 & 0 & 0\end{bmatrix}\begin{bmatrix}\boldsymbol{u}'\\ \boldsymbol{v}'\\ \lambda'\end{bmatrix} = \begin{bmatrix}\partial_{\boldsymbol{u}}\mathcal{S}\\ \partial_{\boldsymbol{v}}\mathcal{S}\\ \partial_{\lambda}\mathcal{S}\end{bmatrix} \tag{2.37}
$$

Hence, for $\mathbf{z} = (\boldsymbol{u},\boldsymbol{v},\lambda)$, and a skew-symmetric matrix K, the multi–symplectic formulation can be written as

$$
K\mathbf{z}_s = \nabla_{\mathbf{z}}\mathcal{S}, \tag{2.38}
$$

The multi–symplectic formulation calculated in this section corresponds to the formulation for a dynamic problem presented in Celledoni and Säfström (2010) with time variables

zero. Constraint $g(\mathbb{q}) = 0$ ensures the solution stays on the surface of sphere, but since $\mathbb{v} \in T^*S^3$ we need another constraint to ensure $\mathbb{v}$ stays on the co-tangent bundle. To find the hidden constraint, differentiating $g(\mathbb{q}) = 0$ once, we get

$$g'(\mathbb{q}) = 2\langle \mathbb{q}, \mathbb{q}' \rangle = 2\langle \mathbb{q}, -\frac{1}{4} R(\mathbb{q}) \widetilde{D}_M^{-1} R(\mathbb{q}^c)\mathbb{v} \rangle = -\frac{\alpha}{2}\langle \mathbb{q}_{id}, R(\mathbb{q}^c)\mathbb{v} \rangle = -\frac{\alpha}{2}\langle \mathbb{q}, \mathbb{v} \rangle,$$
$$\implies g'(\mathbb{q}) = \langle \mathbb{q}, \mathbb{v} \rangle = 0.$$

For $G(\mathbb{q}) = \partial g / \partial \mathbb{q}$, this can be re-written as

$$g'(\mathbb{q}) = G(\mathbb{q})\mathbb{v} = 0, \tag{2.39}$$

The second constraint will ensure $\mathbb{v}$ stays on the co-tangent bundle. We can find the expression for the Lagrange multiplier, by differentiating it again

$$\begin{aligned} g''(\mathbb{q}) &= G'(\mathbb{q})\mathbb{v} + G(\mathbb{q})\mathbb{v}' \\ &= \langle \mathbb{q}', \mathbb{v} \rangle + \langle \mathbb{q}, \mathbb{v}' \rangle \\ &= \lambda + \langle (\epsilon(\mathbb{q}) - \mathbb{1})\boldsymbol{v_x}, D_P^{-1}\boldsymbol{v_x} - \epsilon(\mathbb{q})e_3 \rangle = 0, \end{aligned}$$

$$\implies \lambda = -\langle (\epsilon(\mathbb{q}) - \mathbb{1})\boldsymbol{v_x}, D_P^{-1}\boldsymbol{v_x} - \epsilon(\mathbb{q})e_3 \rangle. \tag{2.40}$$

2.2.4 Twist–Shortening Problem

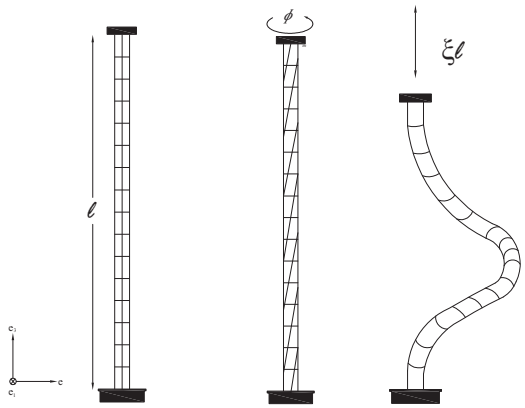

Figure 2.2: Twist–Shortening Explained (Miyazaki and Kondo, 1997)

As discussed in the chapter 1, when a vertically clamped rod is subjected to axial and moment stresses, it can experience deformation in its shape, depending on the configuration of the rod. Suppose such a rod of length l is twisted from one end by an angle ϕ in the positive z-direction and then vertically compressed down by an amount ξl, then it will

experience deformation in its shape, as shown in Figure 2.2. The boundary conditions for this problem will then be

$$Q_0 = \begin{bmatrix} 1 & 0 & 0 \\ 0 & 1 & 0 \\ 0 & 0 & 1 \end{bmatrix}, Q_l = \begin{bmatrix} \cos(\phi) & -\sin(\phi) & 0 \\ \sin(\phi) & \cos(\phi) & 0 \\ 0 & 0 & 1 \end{bmatrix}, \tag{2.41}$$

$$\boldsymbol{x}_0 = \begin{bmatrix} 0 \\ 0 \\ 0 \end{bmatrix}, \boldsymbol{x}_l = \begin{bmatrix} 0 \\ 0 \\ (1-\xi)l \end{bmatrix}.$$

The conditions have been represented using Euler angles but we will use algorithm (1.5) with condition $q_0 > 0$, to find the corresponding Euler parameters in the numerical implementations chapter 4.

Chapter 3

Structure Preserving Geometric Schemes

In the previous chapter, we derived explained the mechanical systems that are considered for the present study. In this chapter, we highlight the essential properties of geometric integrators that are suitable for initial value problems and posses additional geometric structures, e.g preservation of first integrals, energy, and symplecticity. We will later use these methods in combination with shooting techniques (see chapter 4) to solve boundary value problems. Consider a non-autonomous differential equation,

$$\dot{z}(t) = f(t, z(t)), \qquad z(t_0) = z_0. \tag{3.1}$$

The solution is approximated at equally spaced specified points using numerical scheme, suitable for the differential equation. For the present work, we investigate structure preserving geometric integrators based on the class of Runge–Kutta methods. They are used widely for the integration of equations of type (3.1), however many of them do not exhibit properties necessary for the solution. In the next section, we present the numerical schemes for initial value problems that were used in the numerical experiments.

3.1 Initial Value Problem

3.1.1 Runge–Kutta Methods

For an ordinary differential equation (3.1), Runge–Kutta methods take the form

$$K_i = f(t_n + c_i h, z_n + h \sum_{j=1}^{i-1} a_{ij} K_j), \quad \text{for} \quad i = 1, 2, \ldots, s$$

$$\Longrightarrow z_{n+1} = z_n + h \sum_{i=1}^{s} b_i K_i,$$

where s represents the stages and the coefficients are selected from Butcher tableau shown in Table 3.1.

c_1	a_{11}	a_{12}	$\cdots$	a_{1s}
c_2	a_{21}	a_{22}	$\cdots$	a_{2s}
$\vdots$	$\vdots$	$\vdots$	$\ddots$	$\vdots$
c_s	a_{s1}	a_{s2}	$\cdots$	a_{ss}
	b_1	b_2	$\cdots$	b_s

Table 3.1: Butcher tableau

For this thesis, an order 4 Runge–Kutta (RK4) with coefficients shown in Table 3.2 and an order 4 collocation method based on Gauss–Legendre quadrature (GL4) with coefficients shown in Table 3.3 are considered. Both methods are higher order, but the collocation methods have better structure preserving properties in comparison with the RK4. Section 1.3 gives an introduction to first integrals, and their preservation for Runge–Kutta methods is proved in Theorem 3.1.1 and 3.1.2.

0	0	0	0	0
1/2	1/2	0	0	0
1/2	0	1/2	0	0
1	0	0	1	0
	1/6	1/3	1/3	1/6

Table 3.2: Butcher tableau RK4

$\frac{1}{2} - \frac{\sqrt{3}}{6}$	$\frac{1}{4}$	$\frac{1}{4} - \frac{\sqrt{3}}{6}$
$\frac{1}{2} + \frac{\sqrt{3}}{6}$	$\frac{1}{4} + \frac{\sqrt{3}}{6}$	$\frac{1}{4}$
	$\frac{1}{2}$	$\frac{1}{2}$

Table 3.3: Butcher tableau GL4

Theorem 3.1.1. *All explicit and implicit Runge–Kutta methods conserve linear invariants (Marsden and Ratiu, 2013).*

Proof. Suppose a general linear invariant $\mathcal{I}(z) := d^T z$, and a general Runge–Kutta method given by

$$z_{n+1} = z_n + h \sum_{i=1}^{s} b_i K_i, \quad \text{where} \quad K_i = f(z_n + h \sum_{j=1}^{i-1} a_{ij} K_j).$$

Using definition of an invariant, $\nabla \mathcal{I}(z)^T = d^T \implies d^T f(z) = 0$ and also $d^T K_i = 0$. Multiplying the Runge–Kutta method by d^T from the right hand side

$$d^T z_{n+1} = d^T z_n + h \sum_{i=1}^{s} b_i d^T K_i = d^T z_n,$$
$$\implies d^T z_{n+1} = d^T z_n.$$

□

Theorem 3.1.2. *Runge–Kutta methods with coeffecients* $\{c_i\}_{i=1,\dots,s}$, $\{b_i\}_{i=1,\dots,s}$ *and* $\{a_{ij}\}_{i,j=1,\dots,s}$ *satisfying*

$$b_i a_{ij} + b_j a_{ji} = b_i b_j, \quad \textit{for all } i, j \tag{3.2}$$

preserve quadratic invariants.

Proof. Suppose a quadratic invariant of the form $\mathcal{Q}(z) := z^T A z$, written with a general Runge–Kutta scheme as,

$$z_{n+1}^T A z_{n+1}^T = (z_n + h\sum_{j=1}^{s} b_j K_j)^T A (z_n + h\sum_{i=1}^{s} b_i K_i),$$

$$z_{n+1}^T A z_{n+1}^T = z_n^T A z_n + h\sum_{i=1}^{s} b_i z_n^T A K_i + h\sum_{j=1}^{s} b_j K_j^T A z_n + h^2 \sum_{i,j=1}^{s} b_i b_j K_j^T A K_i.$$

From the definition of quadratic invariant we have

$$\nabla \mathcal{Q}(z_{n+1})^T A f(z_{n+1}) = 0 \implies (z_n + h\sum_j a_{ij} K_j)^T A f(z_n + h\sum_j a_{ij} K_j) = 0.$$

Using the identity, $z_n = z_n + h\sum_j a_{ij} K_j - h\sum_j a_{ij} K_j$ and result of quadratic invariant, we simplify,

$$z_{n+1}^T A z_{n+1}^T = z_n^T A z_n - h^2 \sum_{i,j=1}^{s} b_i a_{ij} K_j^T A K_i - h^2 \sum_{i,j=1}^{s} b_j a_{ji} K_j^T A K_i + h^2 \sum_{i,j=1}^{s} b_i b_j K_j^T A K_i,$$

$$z_{n+1}^T A z_{n+1}^T = z_n^T A z_n + h^2 \Big(\sum_{i,j=1}^{s} (-b_i a_{ij} - b_j a_{ji} + b_i b_j) K_j^T A K_i \Big).$$

From this, it follows that quadratic invariant is satisfied only if Equation (3.2) holds. □

Theorem 3.1.3. *If the coeffcients of Runge–Kutta methods satisfy Equation (3.2), then the Runge–Kutta method is symplectic (Hairer et al., 2006).*

From the above two theorems, it is deduced that all Runge–Kutta methods preserve linear invariants but only a subclass of Runge–Kutta methods preserves quadratic invariants. However, invariants greater than or equal to degree 3 are not preserved. (Leimkuhler and Reich, 2004; Hairer et al., 2006; Marsden and Ratiu, 2013; Burden and Faires, 2010)

3.1.2 Midpoint Method

The midpoint method is a second–order Runge–Kutta method used for solving ODEs of type (3.1). The explicit midpoint method (EM) is also known as the modified Euler method, whereas the implicit midpoint method (IM) is the most simple form of collocation

method. Coefficients for the EM and IM are shown in Table (3.4) and (3.5), respectively. Using these coefficients, we can write the numerical scheme for the Equation (3.1).

0	0	0
1/2	1/2	0
	0	1

Table 3.4: Butcher tableau EM

1/2	1/2
	1

Table 3.5: Butcher tableau IM

Let f be a vector field defined on an open subset of a vector space; then the IM can be defined as a mapping from $z_n \mapsto z_{n+1}$,

$$\frac{z_{n+1} - z_n}{h} = f(z_{n+1/2}), \quad \text{where} \quad z_{n+1/2} = \frac{z_{n+1} + z_n}{2}. \tag{3.3}$$

Rearranging the above equation,

$$z^{n+1} = z_n + hf(z_{n+1/2}), \quad \text{where} \quad z_{n+1/2} = \frac{z_{n+1} + z_n}{2}.$$

Similarly, EM can be defined as a mapping from $z_n \mapsto z_{n+1}$ such that,

$$\frac{z_{n+1} - z_n}{h} = f(z_n + \frac{h}{2} f(z_n)). \tag{3.4}$$

IM is symmetric, unconditionally stable, and symplectic for constant symplectic structures. If the symplectic structures are not constant, such as in spin systems, then IM is not symplectic (Hairer et al., 2006; McLachlan et al., 2014). Preservation of linear invariants for EM and IM is followed from Theorem 3.1.1, however quadratic invariants are only preserved by the later.

Proposition 6. *The implicit midpoint method preserves quadratic invariants.*

Proof. Consider the differential equation (3.1), with first integral of the form

$$I(z) = \frac{1}{2} z^T A z + b^T z, \quad \text{such that}$$
$$\frac{d}{dt} I = (Az + b)^T f(z) = 0.$$

Multiply (3.3) by $(Az_{n+1/2} + b)^T$ from the left, and using $(Az + b)^T f(z) = 0$ we get

$$\begin{aligned}(Az_{n+1/2} + b)^T z_{n+1} &= (Az_{n+1/2} + b)^T z_n + h(Az_{n+1/2} + b)^T f(z_{n+1/2}), \\ &= (Az_{n+1/2} + b)^T z_n.\end{aligned}$$

Since, $\frac{(Az_n)^T z_{n+1}}{2} = \frac{(Az_{n+1})^T z_n}{2}$ therefore we can write the above equation as

$$\frac{(z_{n+1})^T A z_{n+1}}{2} + b^T z_{n+1} = \frac{(z_n)^T A z_n}{2} + b^T z_n.$$

This implies that implicit midpoint method preserves quadratic invariants (Leimkuhler and Reich, 2004, page 90). □

3.1.3 Spherical Midpoint Method

The idea behind spherical midpoint method (SM) comes from the implicit midpoint method. Implicit midpoint method is extensively used in computational physics due to its striking properties as explained earlier, however, the method is not symplectic when applied to spin systems (McLachlan et al., 2014). Despite this, it still has been used in many cases due to many other properties, such as spin length preservation, linear stability for all h, etc. The spherical midpoint method coincides with the implicit midpoint method, when applied to the following vector field

$$\rho(z) = f\left(\frac{z_1}{||z_1||}, ..., \frac{z_n}{||z_n||}\right).$$

Spherical midpoint method also proves to have several useful properties. It is second-order accurate, self-adjoint, symplectic and preserves linear first integral and symmetries. If the Hamiltonian is of the form (2.10), then it conserves the quadratic invarian (McLachlan et al., 2014).

3.1.4 Kahan Method

Consider a system of differential equations with initial condition $z(0) = z_0$, arising from quadratic vector fields

$$\dot{z} = f(z) := Q(z) + B(z) + b, \quad \text{for z} \in \mathbb{R}^n, \tag{3.5}$$

where $Q \in \mathbb{R}^n$ is real-valued quadratic form, $B \in \mathbb{R}^{n\times n}$ and $c \in \mathbb{R}^n$. This scheme was introduced by Kahan (1993) for Lotka Volterra system and Riccati equation and written in the general form as (Kahan and Li, 1997)

$$\frac{z_{n+1} + z_n}{h} = Q(z_n, z_{n+1}) + \frac{1}{2}B(z_n + z_{n+1}) + b, \tag{3.6}$$

where,

$$Q(z_n, z_{n+1}) = \frac{1}{2}\left(Q(z_n + z_{n+1}) - Q(z_n) - Q(z_{n+1})\right). \tag{3.7}$$

The method is symmetric and linearly implicit. It is called an "unconventional method" as each term is treated differently. As noted by Kahan and Li (1997), Kahan method has the following property:

Proposition 7. *The Kahan method (3.5) coincides with the Runge–Kutta method,*

$$\frac{z_{n+1} - z_n}{h} = -\frac{1}{2}f(z_n) + 2f\left(\frac{z_{n+1} + z_n}{2}\right) - \frac{1}{2}f(z_{n+1}),$$

restricted to the quadratic vector field (Celledoni et al., 2012).

Proof. Consider discretization for Kahan method (3.6),

$$\begin{aligned}\frac{z_{n+1}+z_n}{h} &= \frac{1}{2}\left(Q(z_n+z_{n+1})-Q(z_n)-Q(z_{n+1})\right)+\frac{1}{2}B(z_n+z_{n+1})+b,\\ &= \frac{1}{2}\left(4Q(\frac{z_n+z_{n+1}}{2})-Q(z_n)-Q(z_{n+1})\right)\\ &\qquad -\frac{1}{2}B(z_n)-\frac{1}{2}B(z_{n+1})+\frac{1}{2}B(\frac{z_n+z_{n+1}}{2})+b,\\ &= -\frac{1}{2}f(z_n)+2f\left(\frac{z_{n+1}+z_n}{2}\right)-\frac{1}{2}f(z_{n+1}).\end{aligned}$$

□

Since all Runge–Kutta methods preserve linear first integrals (Theorem 3.1.1), as a consequence Kahan method also preserves linear first integrals. However, the method is not sympelctic. It is second order accurate for general quadratic fields and does not preserve quadaratic invariants. See Celledoni et al. (2012) for geometric properties of Kahan method.

3.1.5 Symplectic Euler

Given a constrained Hamiltonian system (Hairer et al., 2006, Chap. VII)

$$\begin{aligned}\dot{u} &= H_v(u,v),\\ \dot{v} &= -H_u(u,v)-G(u)^T\lambda,\\ 0 &= g(u)\end{aligned} \tag{3.8}$$

where H is the Hamiltonian of the system and $G(u)=\partial g/\partial u$. Differentiating the constraint $g(u)=0$ with respect to time, we find the second constraint $G(u)H_u(u,v)=0$ (Hairer et al., 2006) that ensures v stays on the cotangent bundle $T^*\mathcal{Q}$ where $\mathcal{Q}=\{u : g(u)=0\}$ is the configuration manifold $\mathcal{M}$ and the manifold is given by $\mathcal{M}=\{(u,v) : g(u)=0, G(u)H_u(u,v)=0\}$. A first order symplectic Euler (SE) scheme can be formulated as follows

$$\hat{v}_{n+1} = v_n - h\Big(H_u(u_n,v_{n+1})+G(v_n)^T\lambda_{n+1}\Big), \tag{3.9}$$

$$u_{n+1} = u_n + hH_v(u_n,\hat{v}_{n+1}), \tag{3.10}$$

$$0 = g(u_{n+1}) \tag{3.11}$$

It is observed that $(\hat{v}_{n+1},u_{n+1})$ satisfies the constraint $g(u)=0$, however the second constraint $G(u)H_u(u,v)=0$ is not satisfied, which means the solution is not the manifold $\mathcal{M}$. In order to bring the solution back to the manifold, a projection technique (shown in Figure 3.1) is incorporated into the solution that ensures the solution stays on the manifold.

$$v_{n+1} = \hat{v}_{n+1} - hG(v_{n+1})^T\mu_{n+1}, \tag{3.12}$$

$$0 = G(v_{n+1})H_v(u_{n+1},v_{n+1}), \tag{3.13}$$

The parameters λ_{n+1} is chosen such that Equation (3.11) is satisfied, i.e

$$g(\mathfrak{q}_{n+1}) = g(\mathfrak{q}_n + hH_{\mathfrak{v}}(u_n, \hat{v}_{n+1})) = 0$$

On the other, the parameter μ_{n+1} is chosen at time step t_n, such that Equation (3.13) is satisfied. It can be proved that the method is order 1, is symplectic however the method is not symmetric (Hairer et al., 2006).

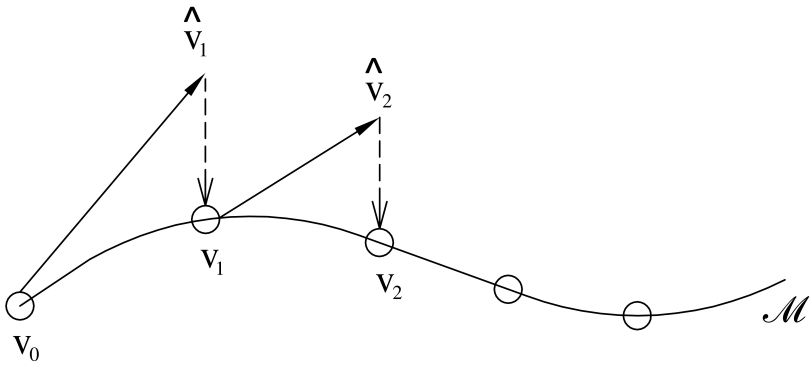

Figure 3.1: Projection Explained

3.1.6 RATTLE Method

A second order symplectic method for (3.8), which is also symmetric known as the RATTLE method (Hairer et al., 2006; Leimkuhler and Reich, 2004) is presented here. It is an extension of a similar algorithm SHAKE, and is used for the integration of equations of motion in molecular dynamics, that are subjected to some constraints. It is advantageous over the SHAKE algorithm, as it satisfies the constraints at each time-step (Andersen, 1983).

$$\begin{aligned}
v_{n+1/2} &= v_n - \frac{h}{2}\Big(H_u(u_n, v_{n+1/2}) + G(u_n)^T\lambda_n\Big),\\
u_{n+1} &= u_n + \frac{h}{2}\Big(H_v(u_n, v_{n+1/2}) + H_v(u_{n+1}, v_{n+1/2})\Big),\\
0 &= g(u_{n+1}),\\
v_{n+1} &= v_{n+1/2} - \frac{h}{2}\Big(H_u(u_{n+1}, v_{n+1/2}) + G(u_{n+1})^T\mu_n\Big),\\
0 &= G(u_{n+1})H_v(u_{n+1}, v_{n+1}).
\end{aligned} \tag{3.14}$$

The first three equations of (3.14) are similar to Equations (3.9), (3.10), (3.11), and the last two are similar to the projection used in symplectic Euler, therefore the Lagrangian multipliers λ_n and μ_n are selected using the same procedure discussed above.

3.2 Boundary Value Problem

Boundary value problems can be numerically solved using finite differences, finite element, or a method that we will be using called the shooting method. Shooting method treats a boundary value problem as an initial value problem and uses integrators discussed in section 3.1 and root finding techniques to find the solution. In this section, we present the fundamental idea behind the shooting method and its extension to time-independent problems such as deformations in space curved beams (subsection 2.2.1).

3.2.1 Shooting Method

Consider a nonlinear second-order ordinary differential equation

$$\ddot{z} = f(x, z, \dot{z}), \qquad a \leq x \leq b, \;\; z(a) = \alpha, \;\; z(b) = \beta, \tag{3.15}$$

where $f(x, z)$ is continuous, differentiable and,

$$\frac{\partial f}{\partial z}(x, z, \dot{z}) \geq 0, \;\; a \leq x \leq b.$$

The first step involves writing second order differential equation into two first order ordinary differentiable equations and varying the angle of inclination (t_k) till the solution at the end point equals the boundary value, i.e

$$\begin{aligned} \dot{z} &= z_1, & z(a) &= \alpha, \\ \dot{z_1} &= f(x, z, z_1), & z_1(a) &= t_0. \end{aligned} \tag{3.16}$$

Suppose $z(x, t_0)$ is the solution the problem (3.16) at $k = 0$, then t_k is varied using either a secant method or Newton–Raphson method. The stopping criteria for the shooting method is as followed,

$$E(t_k) = y(b, t_k) - \beta \leq \epsilon, \tag{3.17}$$

where ϵ is the desired tolerance. See Endre and Mayers (2003); Burden and Faires (2010) for details.

Chapter 4

Experiments and Results

In this chapter we implement the problems discussed in chapter 2 using integration techniques from chapter 3, and analyze the results. The results presented here were produced using MATLAB 2019a.

4.1 Free Rigid Body

As discussed in chapter 2, a free rigid body is a good starting point for complicated problems, therefore we start by implementing schemes discussed in chapter 3 on a free rigid body problem.

4.1.1 Numerical Setup

A free rigid body problem, with Equations (2.1) and (2.2), is an initial value problem that can be solved using the techniques presented in section 3.1. The implicit and collocation methods have been solved using fixed point iteration at each step with a tolerance of 10^{-10}. We choose the inertia tensor $I = \text{diag}(2, 1, 2/3)$ with following initial values.

$$\boldsymbol{M}_0 = \left[\cos(1.1), 0, \sin(1.1)\right]^T, \quad \mathbb{q}_0 = \left[\cos(\tfrac{\theta}{2}),\, \mathbf{e}_1 \sin(\tfrac{\theta}{2})\right]^T, \tag{4.1}$$

for $\theta = \pi/4$ and $\mathbf{e}_1 = [1, 0, 0]$.

4.1.2 Results and Discussion

Using the initial values (4.1) and implicit midpoint method, the solution for the free rigid body in terms of angular momentum can be seen in Figure 4.1, while Figure 4.2 shows the convergence plots for the considered integrators and Table 4.1 shows the convergence rates calculated using polynomial curve fitting tool `polyfit`. The reference solution has been calculated for a small grid-size, i.e $N = 1500$ grid points and the convergence rate achieved matches the theoretical convergence mentioned in chapter 3. In subsection 2.1.3,

the importance of two quadratic invariant quantities was discussed. We have tested the performance of selected geometric integrators on the basis of preservation of invariants. For example, the error in preservation of invariant $\boldsymbol{M}^T\boldsymbol{M}$ has been calculated by subtracting the value at each time step from the value at t_0, i.e

$$E_i = \boldsymbol{M}_i^T\boldsymbol{M}_i - \boldsymbol{M}_0^T\boldsymbol{M}_0, \quad \text{for} \quad i = 1, 2, \ldots, N \tag{4.2}$$

where E_i is the error. As can be seen in Figure 4.3 (a) and Figure 4.3 (b), optimal preservation has been observed for spherical midpoint method, 4th order Gauss–Legendre method, and implicit midpoint method with an accuracy of 10^{-10} to 10^{-14} in contrast to 4th-order Runge–Kutta and Kahan method, that did not give optimal preservation. The accuracy achieved for IM, SM and GL4 is close to the tolerance used for the fixed point iteration, and GL4 being a higher order method has showed the best preservation among all. However, when the tolerance was further reduced to 10^{-13} (see Appendix (A.1) for Figures), IM and GL4 preserved both invariants within the accuracy of 10^{-13} to 10^{-15} (close to the tolerance), but SM outperformed them with an accuracy of 10^{-15} to 10^{-16}. Although, SM showed best preservation among all, but more fluctuations have been observed in comparison to IM and GL4.

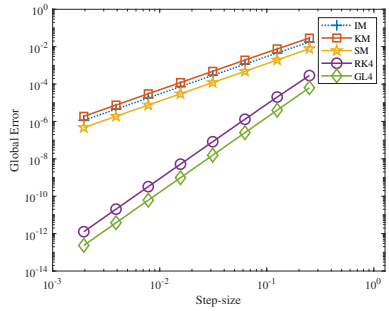

Figure 4.2: Convergence Free Rigid Body

Numerical Scheme	Convergence Rate
IM	1.98
KM	1.98
SM	2.00
RK4	3.94
GL4	4.00

Table 4.1: Convergence Rates

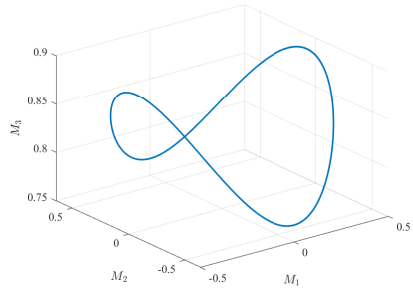

Figure 4.1: Angular momentum calculated using IM. $Tol = 10^{-10}$, $h = T/2^{13}$ and $T = 1000$.

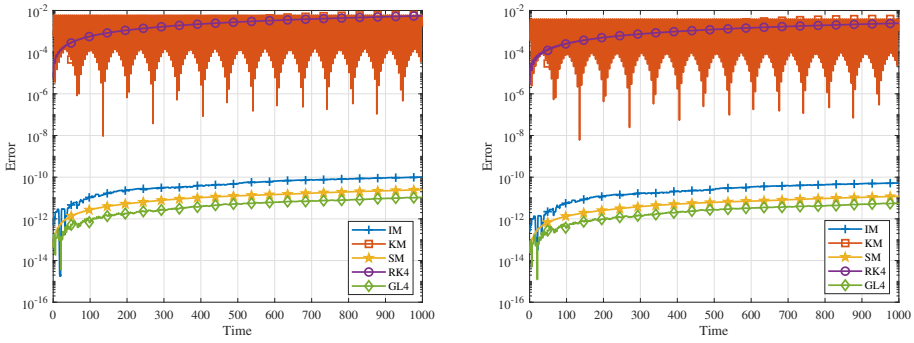

(a) Invariant: $\boldsymbol{M}^T\boldsymbol{M}$ **(b)** Invariant: $\frac{1}{2}\boldsymbol{M}^T I^{-1}\boldsymbol{M}$

Figure 4.3: Error in the preservation of invariants. $Tol = 10^{-10}$, $h = T/2^{13}$ and $T = 1000$.

In the next section, we numerically simulate the deformations in space–curved beams using similar techniques as in the free rigid body problem combined with shooting method.

4.2 Twist-Shortening using Equilibrium Equations

4.2.1 Numerical Setup

Suppose the line of centroid is discretized into N equally spaced grid points with step-size $h = l/N$, as shown in Figure 4.4. Each grid point can be thought of as a particle that is free to roam in 3-dimensional space and using time integrating schemes it is possible to predict the trajectory made by the particle. Since boundary conditions need to be imposed at the end point of the grid, we have used the shooting method as described in subsection 3.2.1 to counter this problem. We do this by setting up an error function

$$E(\mathbf{v}_0) = [\boldsymbol{x}_N - \boldsymbol{x}_l,\ \mathfrak{q}_N - \mathfrak{q}_l]^T, \tag{4.3}$$

with an initial vector $\mathbf{v}_0 = [\boldsymbol{P}_0,\ \boldsymbol{M}_0]^T$ that uses MATLAB's built–in root finding solver `fsolve` to solve the problem. The implicit/collocation methods have been solved using fixed–point iteration and the tolerance used for `fsolve` and fixed–point iteration is 10^{-10}.

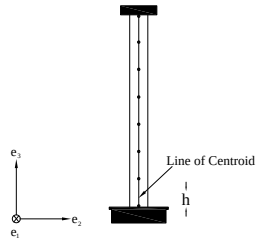

Figure 4.4: Discretization of rod

Cross-sectional properties such as torsional, flexural, shear and extensional rigidity determine how deformations look like after twisting and shortening. For the experiments, cross-sectional properties of a catenary riser (Neto et al., 2014) have been used and are shown in Table 4.2.

Property	Value
Flexural Rigidity (EI)	110.8 MNm^2
Torsional Rigidity (GJ)	85.2 MNm^2
Shear Rigidity (GA)	2,338.6 MN
Extensional Rigidity (EA)	6,080.5 MN
Length (L)	10 m
Diameter (D)	0.4 m

Table 4.2: Cross-sectional properties of rod

4.2.2 Results and Discussion

The rod considered has a cross-sectional area and due to the assumptions mentioned in subsection 2.2.1, and we can examine the deformations by looking at the line of the centroid. The problem has been tested for a twist-shortening problem discussed in subsection 2.2.4. We have tested the accuracy of algorithms by comparing it to a reference solution calculated for the small grid ($N = 2048$) where the error for the schemes is the deviation from the reference solution and has been calculated by its max–norm in the interval $[0, l]$. This is different from the convergence of free rigid body, where 2–norm was used to find the error at the end of the time interval. Figure 4.5 shows the convergence plots and Table 4.3 shows the convergence rates for the selected numerical schemes. Convergence rates have been calculated using the same technique described for the free rigid body problem.

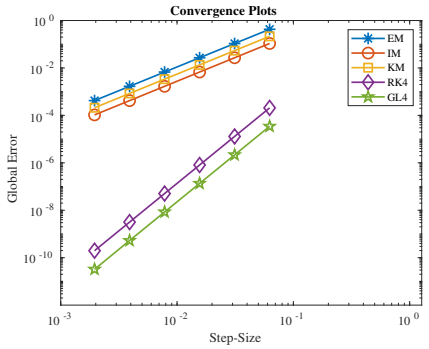

Figure 4.5: Convergence for $\{\phi, \xi\} = \{\pi, 0.5\}$.

Numerical Scheme	Convergence Rate
EM	1.99
IM	2.00
KM	2.00
RK4	4.00
GL4	4.00

Table 4.3: Convergence Rates

We have performed two experiments for the twist-shortening problem. In the first experiment we have varied the angle of twist ϕ and kept ξ constant, while for the second

experiment we only performed axial shortening on the rod, i.e varying ξ and keeping ϕ zero. Results for both experiments can be seen in Figure 4.6 and Figure 4.7, where blue rod is the undeformed rod plotted for reference. When ξ was kept constant, and ϕ varied, the rod started to form a planar loop. With increments in ϕ, the loop showed an increase in the moment strains κ, that matches our assumption (2.16), i.e $M_i \propto \kappa_i^b$. This can be seen in Figure 4.8 (a), that plots moment strain κ_3^b versus angle ϕ varying from 0 to $6\pi/4$. As ϕ is increased, moment strain is also seen increasing, which gives assurance for the quality of the solution.

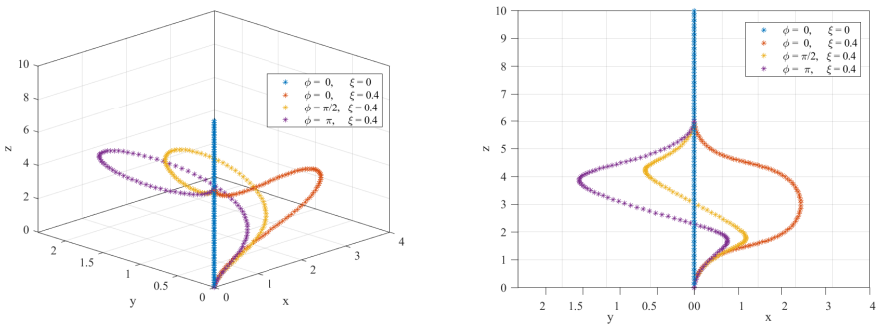

(a) View 1 **(b)** View 2

Figure 4.6: Deformations in line of centroid for varying ϕ and $\xi = 0.4$.

When the rod is subjected to axial shortening with zero twist, a uni-axial compression is observed. In Figure 4.7 (a) we have compressed the rod till $\xi = 0.7$, and when the compression was increased beyond $\xi = 0.8$ a shift of strain energy from bending mode to torsion mode resulted in an instability in the rod, as seen in the Figure 4.7 (b). The reason for this instability is the lack of ability of the rod to further withstand the compression and thus the formation of a kink or a loop with itself. This behavior is justified for a real–life problem, however in the present experiment (only vertical compression) with boundary conditions (2.41), the model has failed to comply with the assumptions (2.16). To test this result, we tested the assumption $P_i \propto \gamma_i^b$ by varying ξ. This can be seen in Figure 4.8 (b), where increase in ξ showed an increase in γ_3^b till $\xi = 0.8$ and on further increase it started to decrease. As a result of this behavior, we call $\xi = 0.8$ as the bifurcation point for this axial compression. This type of behavior is important to study the post–buckling phenomenon in rods. The qualitative structure of our results was validated with the paper Miyazaki and Kondo (1997). Results discussed above were calculated using the implicit midpoint method for $N = 500$ grid points.

We now compare the performance of our selected geometric integrators on the basis of preservation of quantities discussed in subsection 2.2.2. There are three quantities that must be conserved by the integrators, namely $\mathcal{J}$, $\boldsymbol{P}^T\boldsymbol{P}$ and $\boldsymbol{P}^T\boldsymbol{M}$. Using the idea from (4.2), we have similarly checked the error in the preservation of these quantities. As discussed earlier, the solution can either give stable deformations or unstable ones and both cases are important for the study, therefore we test the performance of our integrators in both.

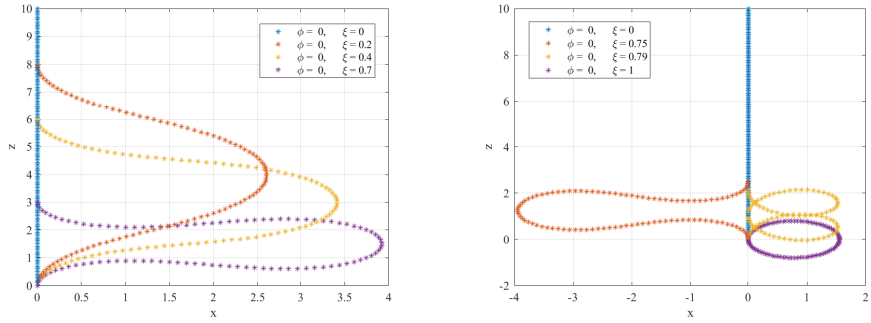

(a) Axial shortening till 0.7 **(b)** Instability for $\xi > 0.8$

Figure 4.7: Deformations in line of centroid for varying ξ and $\phi = 0$.

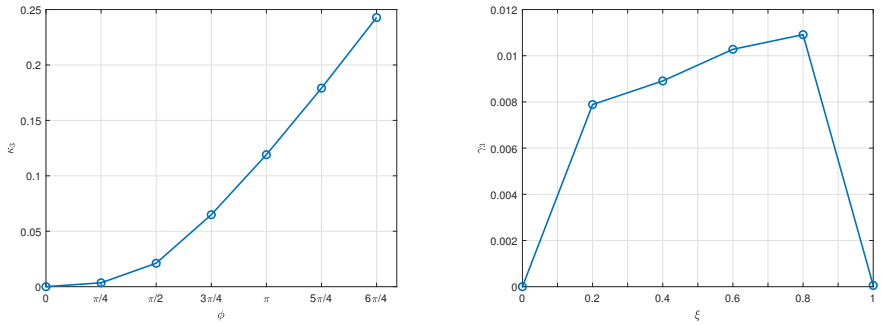

(a) Moment strain (κ_3) for varying ϕ and $\xi = 0.4$ **(b)** Force strain (γ_3) for varying ξ and $\phi = 0$

Figure 4.8: Effect of varying ξ and ϕ on strains.

Case 1

With the parameters ($\{\phi, \xi\} = \{\pi, 0.4\}$) that ensures stable deformations in the rod, 4th order Gauss–Legendre have outperformed all other methods with an accuracy ranging from of 10^{-9} to 10^{-12}, followed by the implicit midpoint method with an accuracy ranging from of 10^{-8} to 10^{-11}. On the other hand, 4th-order Runge–Kutta have shown better performance in comparison to Figure 4.3 with accuracy ranging from 10^{-3} to 10^{-5}. Kahan method and explicit midpoint method are expected to not preserve the conserved quantities and they gave the least accurate preservation with an accuracy ranging from of 10^{-1} to 10^{-2} for stable parameters. These results can be seen in Figure 4.9 (a), Figure 4.10 (a) and Figure 4.11 (a) and the max–norm of the error for each quantity can be seen in Table 4.4.

Remark. The dropping of the error values (in Figure 4.9, Figure 4.10 and Figure 4.11) to 10^{-15}, is due to the integrators giving values close to the machine accuracy.

Case 2

With parameters ($\{\phi, \xi\} = \{0, 0.8\}$) close to the bifurcation point, GL4 and IM have still performed better than the other integrators with an accuracy ranging from 10^{-8} to 10^{-12}, however, their performance was less optimal with more fluctuations when compared to the previous case. This can be seen in Figure 4.9 (b), Figure 4.10 (b) and Figure 4.11 (b). As we see in the Table 4.4, the performance of RK4, KM and EM is affected by the instability. Their performance has significantly reduced for the quantity $\boldsymbol{P}^T\boldsymbol{P}$, whereas the performance for quantities $\boldsymbol{P}^T\boldsymbol{M}$ and $\mathcal{J}$ have improved greatly and is close to the performance of GL4 and IM. The reason for this is related to the physical meaning of quantities $\boldsymbol{P}$ and $\boldsymbol{M}$. As discussed in the section 2.2, $\boldsymbol{P}$ represents the stress resultants responsible for the force strains γ_i^b and $\boldsymbol{M}$ the stress couple responsible for the moment strains κ_i^b, therefore with no twist and only vertical compression, stress resultants are expected to dominate the stress couples when close to the bifurcation point, hence the preservation for $\boldsymbol{P}^T\boldsymbol{P}$ is less optimal for EM, KM and RK4. However, at $\xi = 0.8$, the only strain observed is due to stress resultants and not the stress couple, and $\boldsymbol{P}^T\boldsymbol{M}$ is closer to zero, therefore error in that proximity seen was optimal. This can be seen in Figure 4.10 (b) where almost all methods have dropped close to the machine accuracy. Similarly, since the energy $\mathcal{J}$ is a combination of moment strains and force strains, therefore one observes more fluctuations as shown in Figure 4.11 (b).

Remark. In either of the cases, we have observed that KM, EM and RK4 faced problem in the preservation at the mid interval of the grid points. This is due to the increase in geometrical complexity, however, with a smaller step–size this problem was reduced.

Methods	$\boldsymbol{P}^T\boldsymbol{P}$		$\boldsymbol{P}^T\boldsymbol{M}$		$\mathcal{J}$	
	Stable Parameters	Unstable Parameters	Stable Parameters	Unstable Parameters	Stable Parameters	Unstable Parameters
GL4	1.7×0^{-9}	1.4×10^{-10}	1.4×10^{-10}	3.6×10^{-13}	7.6×10^{-12}	5.3×10^{-12}
IM	4.2×10^{-8}	3.1×10^{-8}	7.3×10^{-9}	6.8×10^{-13}	9.8×10^{-11}	5.9×10^{-11}
RK4	3.5×10^{-5}	2.1×10^{-2}	5.5×10^{-6}	5.4×10^{-13}	4.6×10^{-7}	7.4×10^{-6}
EM	5.6×10^{-1}	1.1×10^{1}	2.5×10^{-1}	1.6×10^{-9}	4.0×10^{-2}	2.0×10^{-2}
KM	5.8×10^{-1}	6.7×10^{0}	2.4×10^{-1}	1.4×10^{-9}	3.6×10^{-2}	1.2×10^{-2}

Table 4.4: Max–norm of the error in the preservation of conserved quantities for stable parameters $\{\phi, \xi\} = \{\pi, 0.4\}$ and unstable parameters $\{\phi, \xi\} = \{0, 0.8\}$.

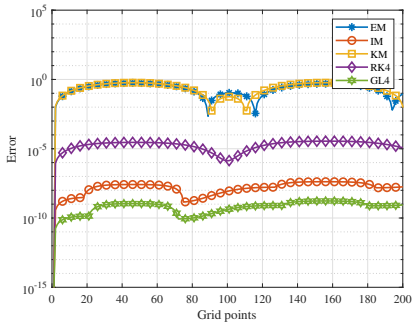

(a) $\{\phi, \xi\} = \{\pi, 0.4\}$

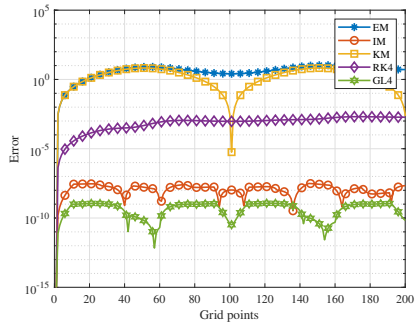

(b) $\{\phi, \xi\} = \{0, 0.8\}$

Figure 4.9: Error in preservation of $\boldsymbol{P}^T\boldsymbol{P}$. $N = 200$, $Tol = 10^{-10}$

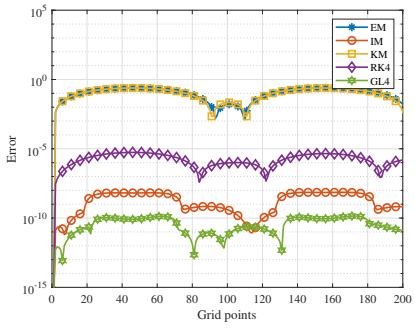

(a) $\{\phi, \xi\} = \{\pi, 0.4\}$

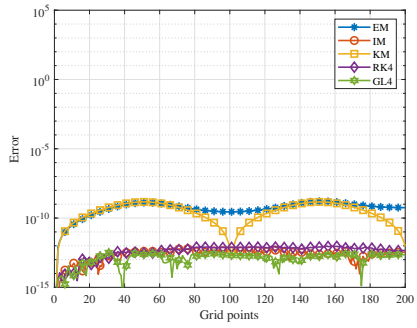

(b) $\{\phi, \xi\} = \{0, 0.8\}$

Figure 4.10: Error in preservation of $\boldsymbol{P}^T\boldsymbol{M}$. $N = 200$, $Tol = 10^{-10}$

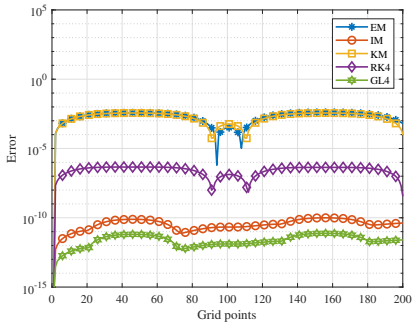

(a) $\{\phi, \xi\} = \{\pi, 0.4\}$

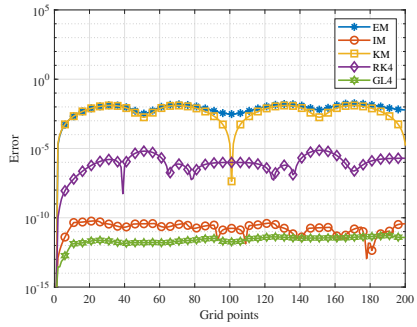

(b) $\{\phi, \xi\} = \{0, 0.8\}$

Figure 4.11: Error in preservation of $\mathcal{J}$. $N = 200$, $Tol = 10^{-10}$

To further understand the effect ϕ and ξ on the preservation of $\mathcal{J}$, $\boldsymbol{P}^T\boldsymbol{P}$ and $\boldsymbol{P}^T\boldsymbol{M}$, we analyze by computing the error in the preservation for varying ϕ and ξ. For any invariant and parameter $\{\phi, \xi\}$ we find the max–norm of the error and plot them using bar–graphs (heights of the bar gives an indication of large/small errors) and charts (containing numeric values of the error). With no axial shortening and only terminal twist, all methods performed optimally due to less complexity in the deformation. However, when only ξ was increased with $\phi = 0$, a degradation in the performance was observed.

It is not expected from KM and EM to preserve the quantities for the cases with both ξ and ϕ not equal to zero, and we see in Figure 4.12 and Figure 4.13 and Figure 4.14, that the error values are substantially large. However, the performance of RK4 is seen better for $\boldsymbol{P}^T\boldsymbol{M}$ and $\mathcal{J}$ but not for $\boldsymbol{P}^T\boldsymbol{P}$. On the contrary, GL4 and IM showed the best preservation properties among all. Figure 4.15, Figure 4.16 and Figure 4.17 gives the values for the max–norm of error and the remaining bar–plots can be found in Appendix (A.2).

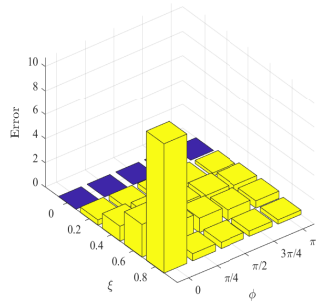

ξ \ ϕ	0	π/4	π/2	3 π/4	π
0	3.94e-59	4.276e-53	7.183e-52	9.212e-51	1.332e-36
0.2	0.441	0.4248	0.3818	0.3236	0.2608
0.4	1.234	1.131	0.9346	0.7377	0.5638
0.6	2.705	1.657	1.192	0.8529	0.5984
0.8	10.68	0.592	0.5201	0.4374	0.3511

Figure 4.12: Max(abs($\boldsymbol{P}_i^T\boldsymbol{P}_i - \boldsymbol{P}_0^T\boldsymbol{P}_0$)), $i = 1, 2, ..N$, using EM for different ξ and ϕ.

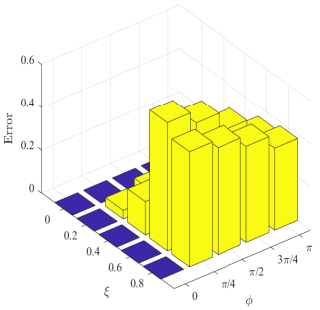

ξ \ ϕ	0	π/4	π/2	3 π/4	π
0	1.891e-54	3.563e-45	7.463e-45	2.764e-44	1.332e-30
0.2	9.055e-11	0.03999	0.07317	0.09593	0.1078
0.4	2.013e-10	0.1547	0.2313	0.2534	0.2484
0.6	2.904e-09	0.5961	0.5377	0.4473	0.3513
0.8	1.609e-09	0.5341	0.4961	0.4452	0.3801

Figure 4.13: Max(abs($\boldsymbol{P}_i^T\boldsymbol{M}_i - \boldsymbol{P}_0^T\boldsymbol{M}_0$)), $i = 1, 2, ..N$, using EM for different ξ and ϕ.

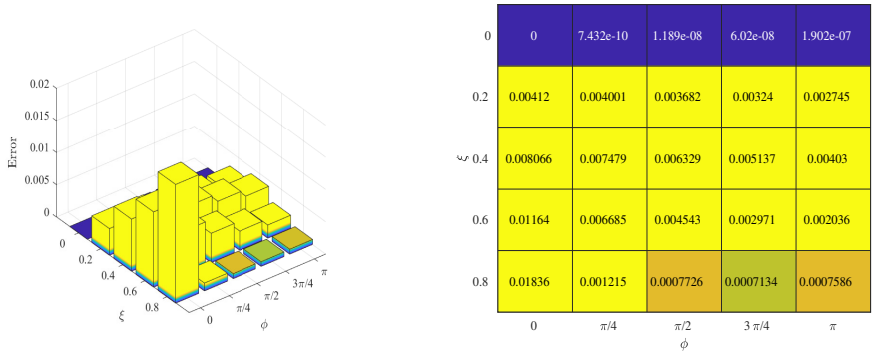

Figure 4.14: Max(abs($\mathcal{J}_i - \mathcal{J}_0$)), $i = 1, 2, ..N$, using EM for different ξ and ϕ.

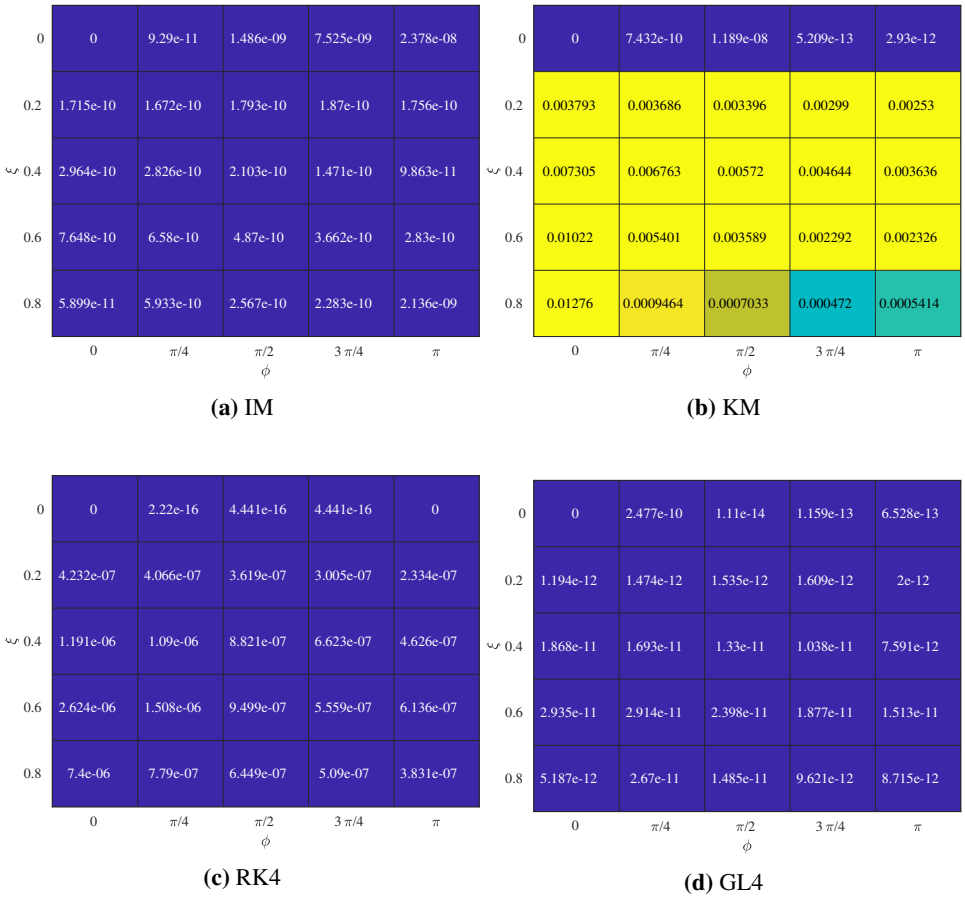

(a) IM **(b)** KM

(c) RK4 **(d)** GL4

Figure 4.17: Values of max(abs($\mathcal{J}_i - \mathcal{J}_0$)) for varying ξ and ϕ.

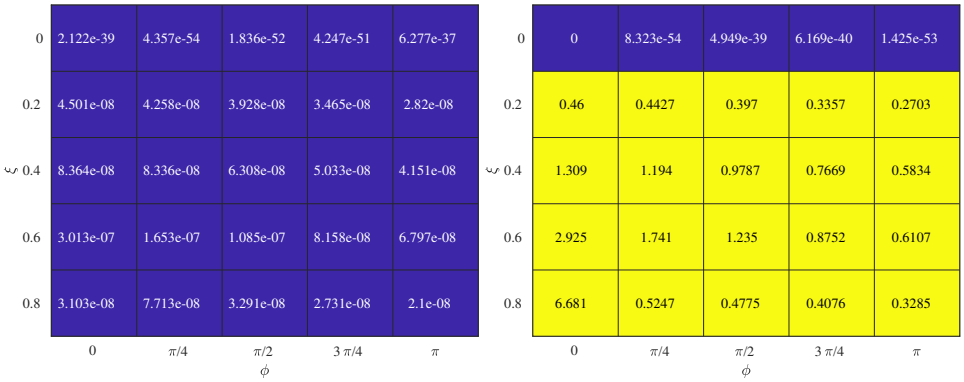

(a) IM **(b)** KM

(c) RK4 **(d)** GL4

Figure 4.15: Values of max(abs($\boldsymbol{P}_i^T\boldsymbol{P}_i - \boldsymbol{P}_0^T\boldsymbol{P}_0$)) for varying ξ and ϕ.

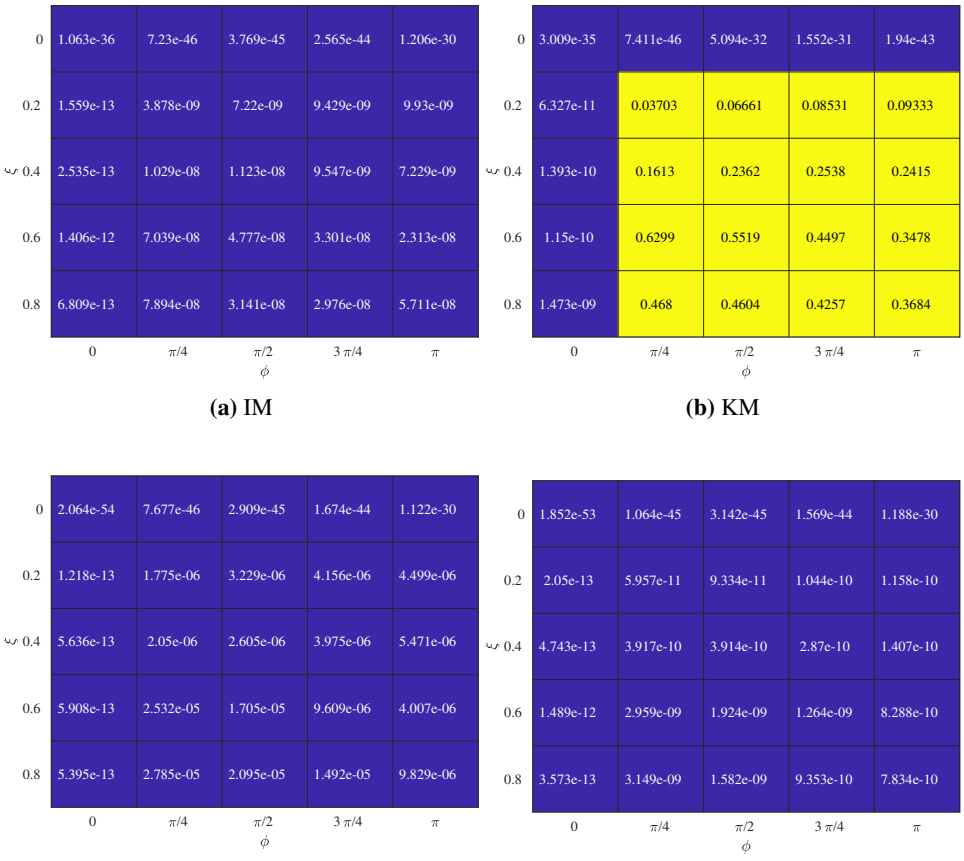

(a) IM **(b)** KM

(c) RK4 **(d)** GL4

Figure 4.16: Values of max(abs($\boldsymbol{P}_i^T \boldsymbol{M}_i - \boldsymbol{P}_0^T \boldsymbol{M}_0$)) for varying ξ and ϕ.

Balance of Linear Momentum

In the previous part, we have investigated the preservation properties of our numerical schemes for the conserved quantities and the results showed optimal performance for higher–order GL4 and second–order IM for both stable and unstable deformations. KM method even though does not preserve any invariants, but it is well known to give completely integrable discretizations when applied to certain completely integrable rigid body systems (Celledoni et al., 2014). Though KM and EM performed closely in the preservation of invariants, but in this experiment we will numerically show that KM is preferable over EM. We will now look at the performance of our numerical schemes for the balance equation of linear momentum (2.22). We rewrite it as follows:

$$\partial_s \boldsymbol{p} = 0, \implies \boldsymbol{p} = Q^T \boldsymbol{P} = \text{Const}$$

And using the expression for quantity $\boldsymbol{P}^T\boldsymbol{P} = \boldsymbol{p}^T\boldsymbol{p} = \text{Const}$, we say that the solution for $\boldsymbol{p}$ will be confined on the surface of sphere as shown in Figure 4.18. We test the performance for the twist–shortening problem using different step–sizes. Figure 4.19 shows the values of $\mathcal{E}(\mathfrak{q}_i)^T\boldsymbol{P}_i$ for $i = 1, 2, ...N$ calculated on a coarser grid with step–size $h = 1$. We observe that EM did not give a closed orbit, in comparison to the other methods as shown in Figure 4.19 (a), however; when the step–size was reduced to $h = 0.5$, the trajectory made for EM started to improve as shown in Figure 4.20 (a). On further refinement of mesh to step–size $h = 0.05$, we observed a smoother trajectory as shown in Figure 4.21 (a).

With parameters ensuring stable deformations, it was difficult to distinguish between the numerical schemes, however, a clear difference was observed for unstable deformations. For coarser grid with step–size $h = 0.5$, a degradation in performance for EM was observed in comparison to the case of stable deformations. Similarly, the performance of IM and KM were also affected as shown in Figure 4.22 (c) and (b), but the trajectories made by higher order methods such as RK4 and GL4 were optimal. On further refinement, a circular ring like trajectory was made for all the methods as shown in Figure 4.23.

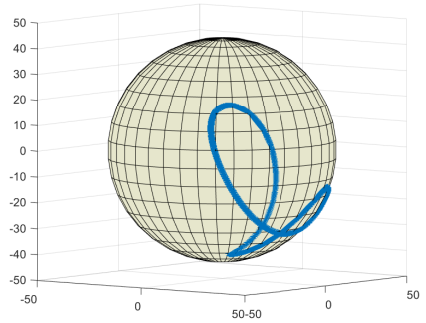

Figure 4.18: $\mathcal{E}(\mathfrak{q}_i)^T\boldsymbol{P}_i$ plotted on sphere for $h = 0.01$ and $\{\phi, \xi\} = \{\pi, 0.4\}$.

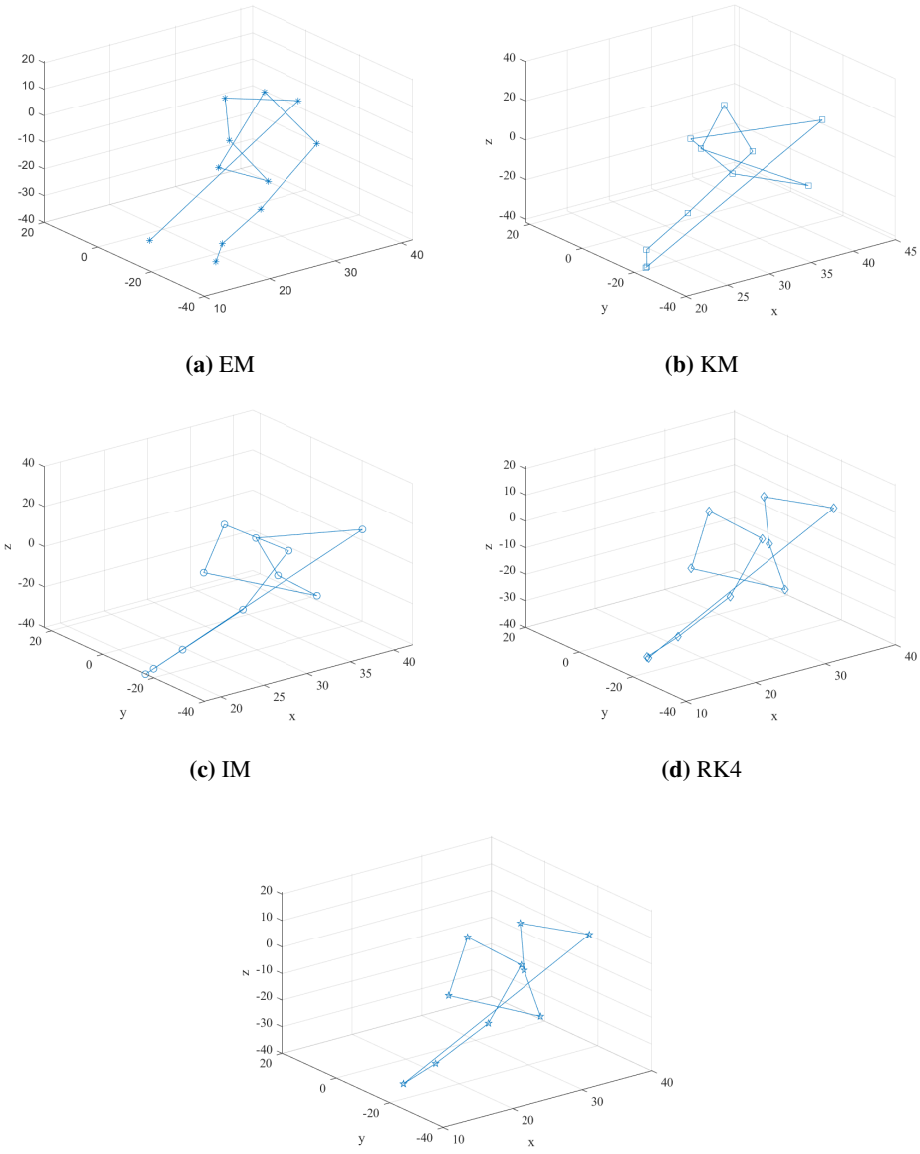

(a) EM

(b) KM

(c) IM

(d) RK4

(e) GL4

Figure 4.19: $\mathcal{E}(\mathbb{q}_i)^T \boldsymbol{P}_i$ for $h = 1$ and $\{\phi, \xi\} = \{\pi, 0.4\}$.

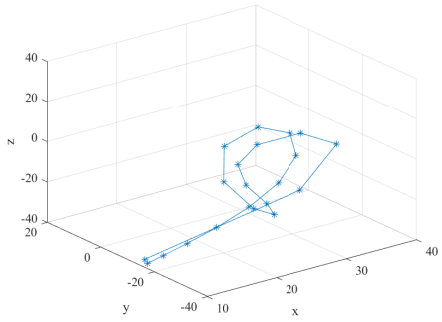

(a) EM

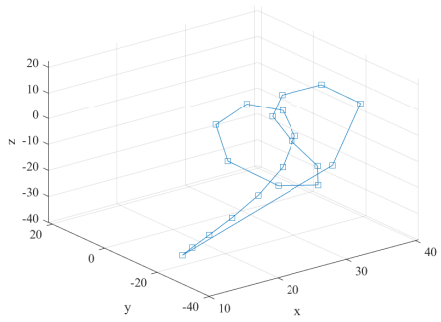

(b) KM

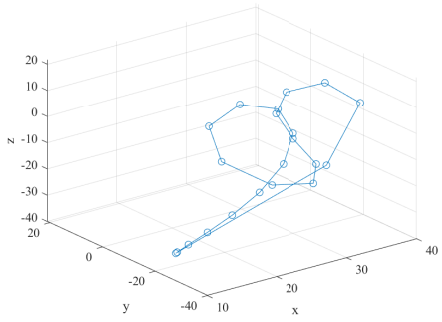

(c) IM

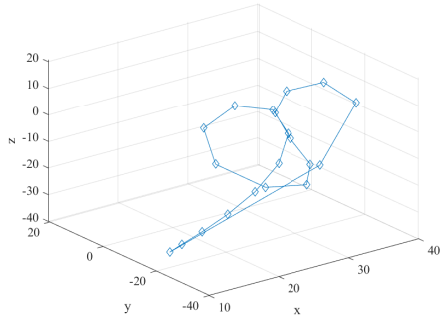

(d) RK4

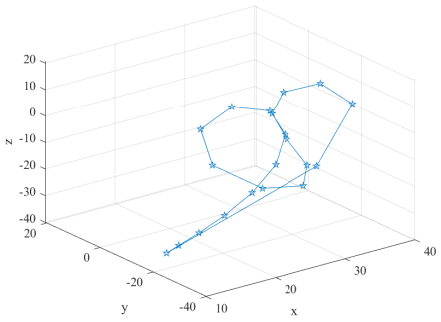

(e) GL4

Figure 4.20: $\mathcal{E}(\mathfrak{q}_i)^T \boldsymbol{P}_i$ for $h = 0.5$ and $\{\phi, \xi\} = \{\pi, 0.4\}$.

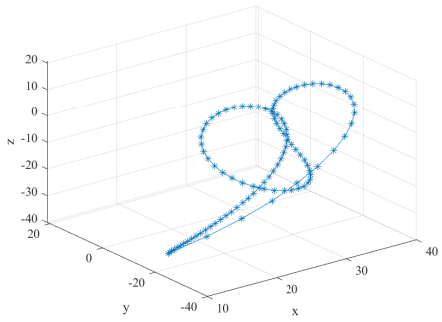

(a) EM

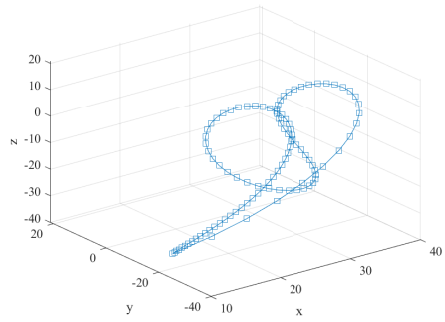

(b) KM

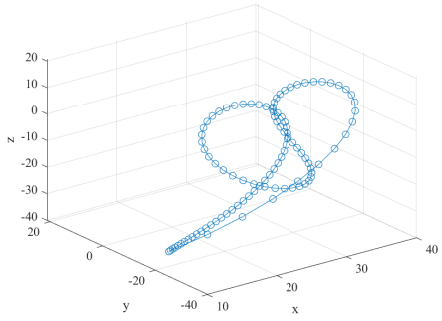

(c) IM

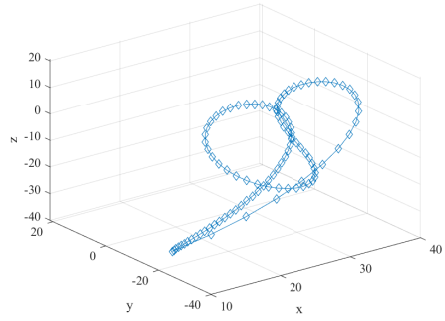

(d) RK4

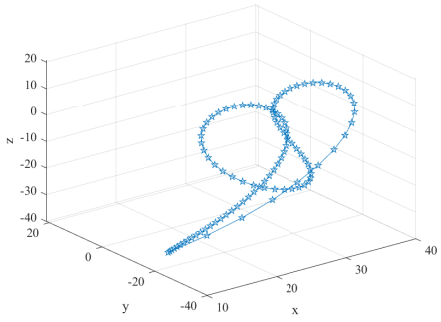

(e) GL4

Figure 4.21: $\mathcal{E}(\mathfrak{q}_i)^T \boldsymbol{P}_i$ for $h = 0.1$ and $\{\phi, \xi\} = \{\pi, 0.4\}$.

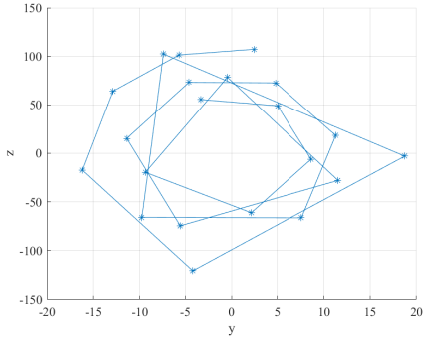

(a) EM

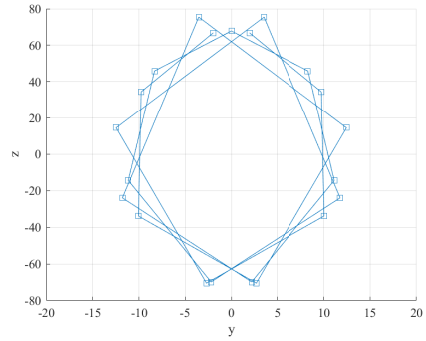

(b) KM

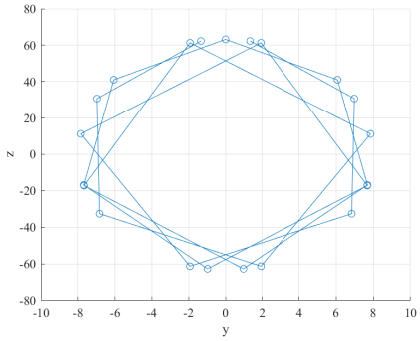

(c) IM

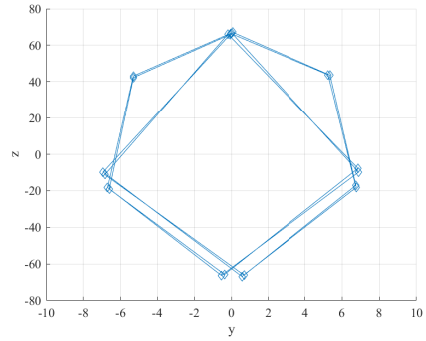

(d) RK4

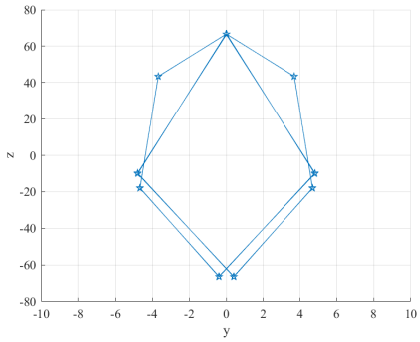

(e) GL4

Figure 4.22: $\mathcal{E}(\mathfrak{q}_i)^T \boldsymbol{P}_i$ for $h = 0.5$ and $\{\phi, \xi\} = \{0, 0.8\}$.

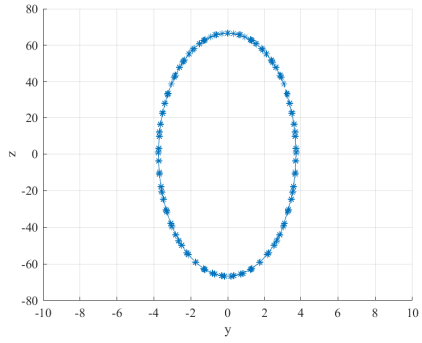

(a) EM

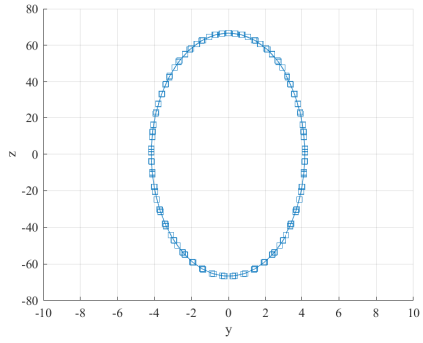

(b) KM

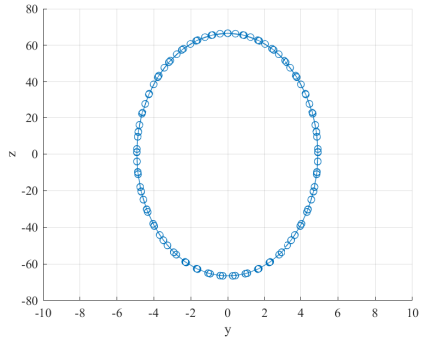

(c) IM

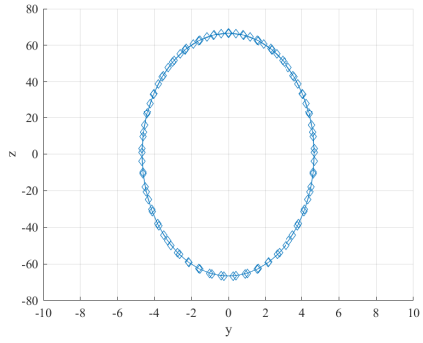

(d) RK4

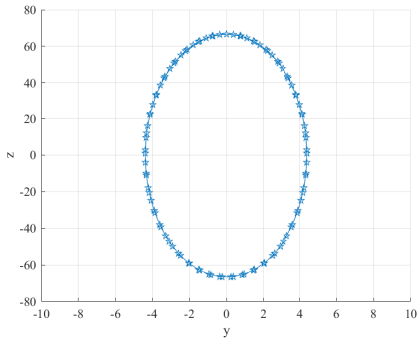

(e) GL4

Figure 4.23: $\mathcal{E}(\mathfrak{q}_i)^T \boldsymbol{P}_i$ for $h = 0.05$ and $\{\phi, \xi\} = \{0, 0.8\}$.

Center of Mass

IM and GL4 methods ensure the length of the quaternions is preserved automatically to machine accuracy, however EM, KM and RK4 do not preserve this invariant. It is possible to normalize quaternion at each step, but then the algorithm will be called projected RK4, KM and EM. Doing this will increase the performance, but there is a possibility of ruining other properties of the method. We will now test grid–size dependence on the trajectory made for the center of mass ($Q^T e_3$). The results are shown in Figure 4.24.

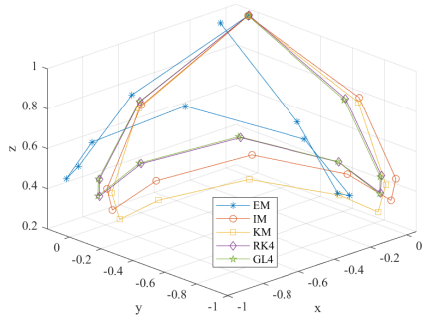

(a) $h = 1$

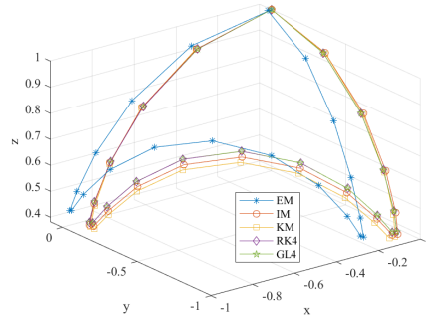

(b) $h = 0.5$

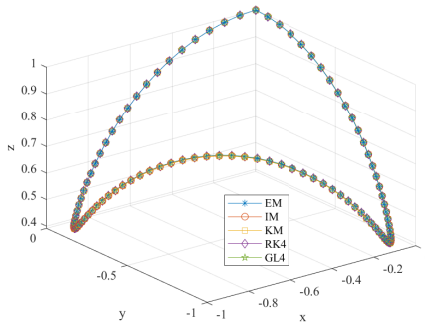

(c) $h = 0.1$

Figure 4.24: Center of mass $(\mathcal{E}(\mathfrak{q}_i)^T e_3)$ for $\{\phi, \xi\} = \{\pi, 0.4\}$.

4.3 Twist-Shortening using Multi-Symplectic Formulation

In the previous section, we performed simulations using the equilibrium equations from subsection 2.2.1 and now we will simulate similar deformations in rods using multi–symplectic formulations. The challenge and aim of this part were to understand and provide an easy explanation for the implementation of symplectic integration techniques for constrained mechanical systems, such as space–curved beams with holonomic constraint.

4.3.1 Numerical Setup

In this section, we present the numerical setup for the implementation of Equations (2.38) using techniques from subsection 3.1.5 and subsection 3.1.6. It is possible to write (2.31) in a way similar to (3.8) as follows:

$$\boldsymbol{u}' = \widetilde{\mathcal{S}}_{\boldsymbol{v}}(\boldsymbol{u}, \boldsymbol{v}), \tag{4.4}$$

$$\boldsymbol{v}' = -\widetilde{\mathcal{S}}_{\boldsymbol{u}}(\boldsymbol{u}, \boldsymbol{v}) - G(\mathbb{q})^T \lambda, \tag{4.5}$$

$$0 = ||\mathbb{q}||^2 - 1, \tag{4.6}$$

where $\widetilde{\mathcal{S}}(\boldsymbol{u}, \boldsymbol{v})$ comes from rewriting (2.31) as, $\mathcal{S}(\boldsymbol{u}, \boldsymbol{v}) = \widetilde{\mathcal{S}}(\boldsymbol{u}, \boldsymbol{v}) + \lambda(||\mathbb{q}||^2 - 1)$ and $G(\mathbb{q}) = 2\mathbb{q}$. There are two techniques possible for the implementations of the multi–symplectic formulation. The first technique called index reduction (Hairer et al., 2006) and uses the expression for λ (2.40) to remove the Lagrangian multiplier from the system (2.38). However, the technique is not feasible as the solution is seen to drift away from the manifold (Hairer et al., 2006; Leimkuhler and Reich, 2004). The use of projection can help the solution to get back to the manifold, but the quality of the solution is then compromised. The second technique is the use of symplectic methods combined with a projection step, where the Lagrangian multipliers λ and μ are selected to impose constraints $g(\mathbb{q}) = 0$ and $\langle \mathbb{q}, \mathbb{v} \rangle = 0$, as discussed in subsection 3.1.5. This approach is preferable over the former one but is more complicated to implement. The Lagrangian multiplier μ_n (for the RATTLE method) is calculated, by ensuring the grid points $n + 1$ (for $n = 1, 2, \ldots, N$.) satisfies (2.39). A detailed calculation for μ_n is as follows:

$$\langle \mathbb{q}_{n+1}, \mathbb{v}_{n+1} \rangle = 0,$$

Using Equation (3.12),

$$\mathbb{q}_{n+1}^T \Big(\mathbb{v}_{n+1/2} - \frac{h}{2} (\widetilde{\mathcal{S}}_{\boldsymbol{u}}(\boldsymbol{u}_{n+1}, \boldsymbol{v}_{n+1/2}) + 2\mathbb{q}_{n+1}\mu_n) \Big) = 0,$$

$$\implies \mu_n = \frac{1}{h} \Big(\mathbb{q}_{n+1}^T \mathbb{v}_{n+1/2} - \frac{h}{2} \widetilde{\mathcal{S}}_{\boldsymbol{u}}(\boldsymbol{u}_{n+1}, \boldsymbol{v}_{n+1/2}) \Big). \tag{4.7}$$

Similarly, the Lagrangian multiplier λ can be calculated by ensuring following condition is satisfied,

$$g(\mathbb{q}_{n+1}) = 0 \implies g(q_n + \frac{h}{2} \widetilde{\mathcal{S}}_{\boldsymbol{v}}(\boldsymbol{u}_n, \boldsymbol{v}_{n+1/2})) = 0, \tag{4.8}$$

The numerical setup for the shooting method uses the same error function (4.3) from the previous section, however the vector $\boldsymbol{v}_0 = [\boldsymbol{P}_0 \ \boldsymbol{M}_0]^T$ is replaced by $\boldsymbol{v}_0 = [\boldsymbol{v}_{\mathbf{x}0} \ \mathbb{v}_0]^T$.

4.3.2 Results and Discussion

As discussed in section 3.1, integrators like as implicit midpoint or higher order Gauss-collocation methods are stable, symplectic and preserve invariants but they can only be exploited in the multi–symplectic setting if position constraints such as (2.36) and (2.39) are satisfied. For ease, we implemented the first-order symplectic Euler implemented using index-reduction and RATTLE method by using Lagrangian multipliers calculated from Equation (4.7) and (4.8). We tested the algorithm against the reference solution calculated using RM for $N = 2048$ grid points. Figure 4.25 shows the convergence plots and Table 4.5 the numeric values for convergence rates calculated using the same technique mentioned in the previous section.

The solution is calculated using RM and SE with multi–symplectic formulation and a reference solution using implicit midpoint on the equilibrium equations from previous section. It is shown in Figure 4.26 (a). It was observed that RM did give a similar solution to the IM but they were not completely identical. To investigate this behavior we checked on how well they preserved constraints. RM ensured the solution to stay on the manifold but the accuracy for constraint (2.39) was 10^{-3} and a drift from the manifold was observed for SE. This explains the large error for SE in Figure 4.25 for large step-sizes.

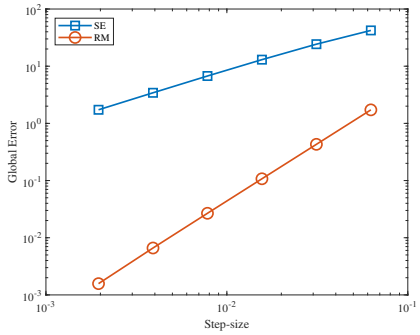

Figure 4.25: Convergence $\{\phi, \xi\} = \{\pi, 0.5\}$

Numerical Scheme	Rate
Symplectic Euler (SE)	0.93
Rattle Method (RM)	2.02

Table 4.5: Convergence Rates

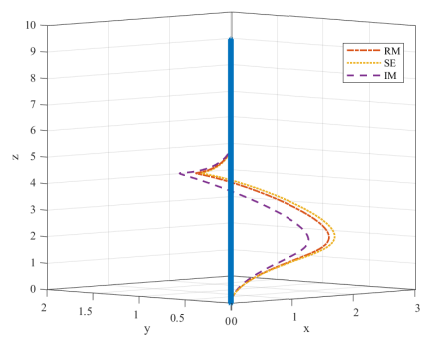

(a) Twist–Shortening for $\{\phi, \xi\} = \{\pi/2, 0.25\}$

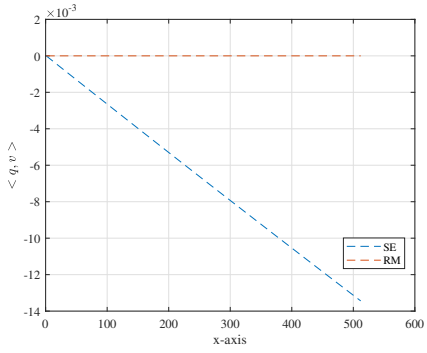

(b) Error in constraint $\langle \mathfrak{q}, \mathfrak{v} \rangle$

Figure 4.26: Solution for twist–shortening using multi–symplectic formulation.

We will now perform the axial shortening on the rod using the equations of multi–symplectic formulation. Figure 4.27 (a) shows the deformations for vertical compression till $\xi = 0.8$ and Figure 4.27 (b) shows the deformations when we try to compress rod completely, i.e $\xi = 1$. When the rod is compressed completely, a loop is formed with both ends joined. This behavior is similar to the results in Miyazaki and Kondo (1997) and provides validation of our results. The axial shortening results calculated using multi–symplectic are also similar to the ones produced in the previous section with an instability for $\xi \geq 0.8$.

Remark. `fsolve` for SE required smaller step–sizes for the convergence.

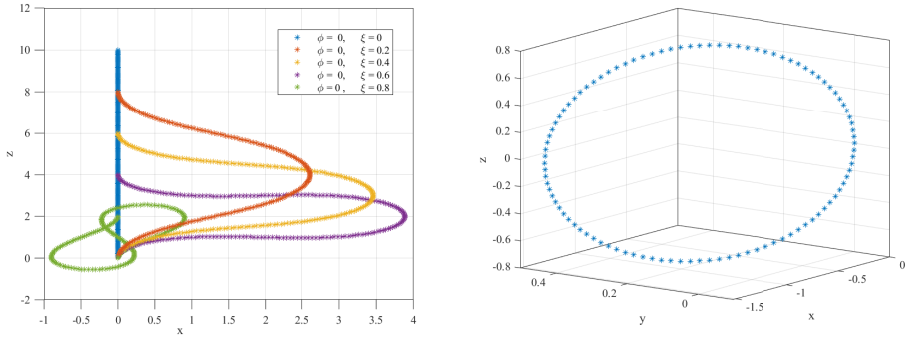

(a) Axial shortening using multi–symplectic

(b) Complete Axial Shortening

Figure 4.27: Solution for twist–shortening using multi–symplectic formulation.

The resulting equations from multi–symplectic formulation does not explicitly contain equations for stress resultants $\boldsymbol{P}$ and stress couple $\boldsymbol{M}$, and quantities that are conserved in the previous formulation might no longer hold in this new setting. Therefore we have not investigated the preservation of conserved quantities and we set them as future work. We however test the RM and SE by plotting the trajectories for the center of mass $Q^T e_3$ with different step–sizes. This can be seen in Figure 4.28. We observe that, when step–size is decreased to $h = 0.001$, trajectory followed by SE is closer to the trajectory followed by RM but it is not exactly equal. In order for the SE to give trajectories identical to RM, one needs a very fine grid.

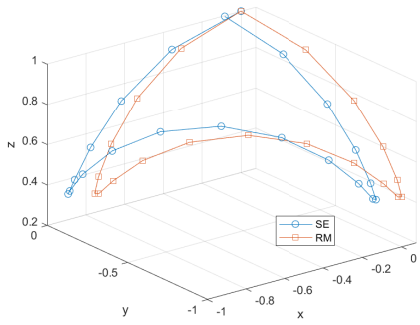

(a) $h = 0.5$

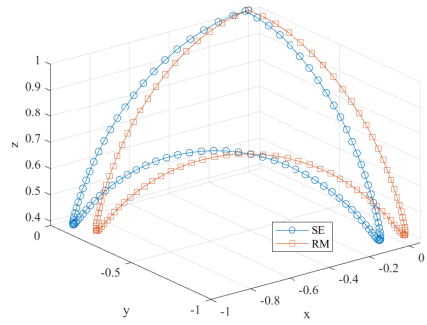

(b) $h = 0.1$

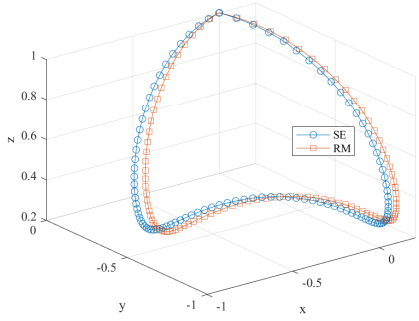

(c) $h = 0.001$

Figure 4.28: Center of mass $(\mathcal{E}(\mathfrak{q}_i)^T e_3)$ for $\{\phi, \xi\} = \{\pi, 0.4\}$ using multi–symplectic for RM and SE.

Chapter 5

Conclusion and Future Work

The goal of this master thesis was to use geometric integration for the simulation of deformations in rods. We had two problems under consideration, a time–dependent free rigid body problem and a time–independent for space–curved beams. We rewrote the equilibrium equations for space–curved beams in compact form using vectors, and then presented a multi–symplectic formulation in chapter 2. Both formulations were applied to a twist–shortening problem and were numerically implemented using geometric integrators presented in chapter 3.

Numerical results for both problems gave convergence rates close to the ones stated in section 3.1 and solutions as anticipated, with some exceptions for the multi–symplectic case. We performed two different experiments on the equilibrium equations. In the first experiment, we looked at the effect of torsion on the moment strains by varying the twist angle and keeping vertical compression constant, whereas in the second experiment, we only performed axial shortening of the rod by applying vertical compression till the bifurcation point. The solutions obeyed assumptions (2.16), for the first experiment, however, it became unstable when the rod was compressed beyond the bifurcation point and failed to satisfy the assumptions for $\xi \geq 0.8$. We also performed a thorough investigation of the performance of structure–preserving schemes for the preservation of conserved quantities and compared them to the non–preserving schemes. GL4 and IM method showed the best preservation of geometric properties among all. However, GL4 being a high order method took more computational time. We also tested all methods for the preservation of balance equation of linear momentum and studied the grid–size dependence on the confinement of solution to the sphere. KM, IM, GL4 and RK4 showed optimal performance for large step–sizes, except for EM.

The limitations associated with the multi–symplectic formulation was only the time taken by the shooting method to converge to the solution, and when tried in the vicinity of unstable points it required very small step-sizes to converge to the solution. Nevertheless, the work presented here can serve as a starting point for understanding multi–symplectic formulations and extensions to the time–dependent problem. The other limitation faced during the implementation was the use of spherical midpoint method on the space–curved

beams. Spherical midpoint showed the best preservation properties among other methods in the free rigid body case. However, it could not be applied on the space–curved beams, because the equation for stress couple in (2.17) is not on the surface of the sphere even though the equation the stress resultant is. A coordinate transformation for transforming the system from Cartesian to a spherical coordinate system could have helped, but that would have complicated the problem. Another limitation in the model is the failure to satisfy assumptions near the post-buckling point. This limitation can be removed by introducing rather an additional boundary condition on the point where the rod forms a loop with itself. The model will then be called a contact problem.

A suggested extension of this work can be to merge the contact problem with the twist–shortening problem, such that whenever rod tries to form a loop with itself, the solution satisfies the assumptions due to the additional conditions. Since stress resultants is on sphere, one could try to formulate a spherical midpoint for $\boldsymbol{P}$. An extension to space–time rod problems is also suggested.

Bibliography

Andersen, H. C., 1983. Rattle: A velocity version of the shake algorithm for molecular dynamics calculations. Journal of Computational Physics 52 (1), 24–34.

Bridges, T. J., 1997. Multi-symplectic structures and wave propagation. In: Mathematical Proceedings of the Cambridge Philosophical Society. Vol. 121. Cambridge University Press, pp. 147–190.

Bridges, T. J., Reich, S., 2001. Multi-symplectic integrators: numerical schemes for hamiltonian pdes that conserve symplecticity. Physics Letters A 284 (4-5), 184–193.

Burden, R. L., Faires, J. D., 2010. Numerical analysis. Cengage Learning 9.

Celledoni, E., Fassò, F., Säfström, N., Zanna, A., 2008. The exact computation of the free rigid body motion and its use in splitting methods. SIAM Journal on Scientific Computing 30 (4), 2084–2112.

Celledoni, E., Høiseth, E. H., Ramzina, N., 2018. Passivity-preserving splitting methods for rigid body systems. Multibody System Dynamics 44 (3), 251–275.

Celledoni, E., McLachlan, R. I., McLaren, D. I., Owren, B., Quispel, G., 2014. Integrability properties of kahans method. Journal of Physics A: Mathematical and Theoretical 47 (36), 365202.

Celledoni, E., McLachlan, R. I., Owren, B., Quispel, G. R. W., 2012. Geometric properties of kahan's method. Journal of Physics A: Mathematical and Theoretical 46 (2), 025201.

Celledoni, E., Säfström, N., 2010. A hamiltonian and multi-hamiltonian formulation of a rod model using quaternions. Computer Methods in Applied Mechanics and Engineering 199 (45-48), 2813–2819.

Coutsias, E. A., Romero, L., 2004. The quaternions with an application to rigid body dynamics.

Egeland, O., Gravdahl, J. T., 2002. Modeling and simulation for automatic control. Vol. 76. Marine Cybernetics Trondheim, Norway.

Endre, S., Mayers, D., 2003. An introduction to numerical analysis. Cambridge, UK.

Green, A. E., Zerna, W., 1992. Theoretical elasticity. Courier Corporation.

Hairer, E., Lubich, C., Wanner, G., 2006. Geometric numerical integration: structure-preserving algorithms for ordinary differential equations. Vol. 31. Springer Science & Business Media.

Kahan, W., 1993. Unconventional numerical methods for trajectory calculations. Unpublished lecture notes 1, 13.

Kahan, W., Li, R.-C., 1997. Unconventional schemes for a class of ordinary differential equationswith applications to the korteweg–de vries equation. Journal of Computational Physics 134 (2), 316–331.

Leimkuhler, B., Reich, S., 2004. Simulating hamiltonian dynamics. Vol. 14. Cambridge university press.

Love, A. E. H., 1944. A treatise on the mathematical theory of elasticity. Cambridge university press.

Maciejewski, A. J., 1985. Hamiltonian formalism for euler parameters. Celestial mechanics 37 (1), 47–57.

Marsden, J. E., Ratiu, T. S., 2013. Introduction to mechanics and symmetry: a basic exposition of classical mechanical systems. Vol. 17. Springer Science & Business Media.

McLachlan, R. I., Modin, K., Verdier, O., 2014. Symplectic integrators for spin systems. Physical Review E 89 (6), 061301.

Miyazaki, Y., Kondo, K., 1997. Analytical solution of spatial elastica and its application to kinking problem. International journal of solids and structures 34 (27), 3619–3636.

Neto, A. G., Martins, C. A., Pimenta, P. M., 2014. Static analysis of offshore risers with a geometrically-exact 3d beam model subjected to unilateral contact. Computational Mechanics 53 (1), 125–145.

Olver, P. J., 2012. Applications of Lie groups to differential equations. Vol. 107. Springer Science & Business Media.

Reissner, E., 1981. On finite deformations of space-curved beams. Zeitschrift für angewandte Mathematik und Physik ZAMP 32 (6), 734–744.

Ringheim, I. M., 2013. Numerical solution of equilibrium equations of spatial elastica. Master's thesis, Institutt for matematiske fag.

Schwab, A. L., 2002. Quaternions, finite rotation and euler parameters. Cornell University Notes, Ithaca NY.

Shepperd, S. W., 1978. Quaternion from rotation matrix.[four-parameter representation of coordinate transformation matrix].

Simo, J., Tarnow, N., Doblare, M., 1995. Non-linear dynamics of three-dimensional rods: Exact energy and momentum conserving algorithms. International Journal for Numerical Methods in Engineering 38 (9), 1431–1473.

Simo, J. C., 1985. A finite strain beam formulation. the three-dimensional dynamic problem. part i. Computer methods in applied mechanics and engineering 49 (1), 55–70.

Simo, J. C., Marsden, J. E., Krishnaprasad, P., 1988. The hamiltonian structure of nonlinear elasticity: the material and convective representations of solids, rods, and plates. Archive for Rational Mechanics and Analysis 104 (2), 125–183.

Simo, J. C., Vu-Quoc, L., 1986. A three-dimensional finite-strain rod model. part ii: Computational aspects. Computer methods in applied mechanics and engineering 58 (1), 79–116.

Appendix A

Error in Preservation of Invariants

A.1 Free Rigid Body

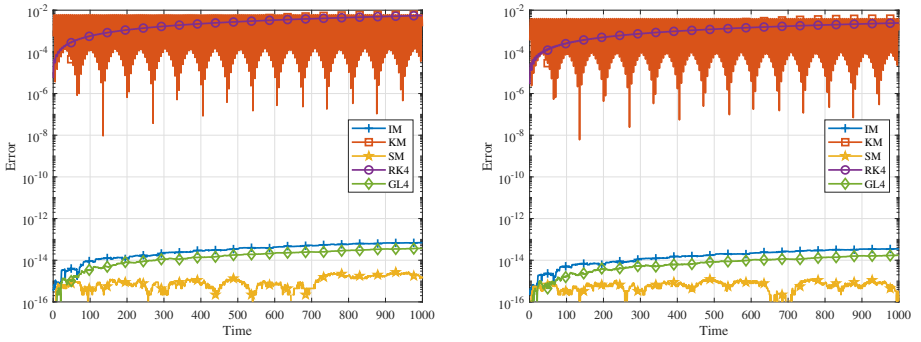

(a) Invariant: $\boldsymbol{M}^T\boldsymbol{M}$

(b) Invariant: $\frac{1}{2}\boldsymbol{M}^T I^{-1}\boldsymbol{M}$

Figure A.1: Error in the preservation of invariants. $Tol = 10^{-13}$, $h = T/2^{13}$ and $T = 1000$.

A.2 Space–Curved Beams

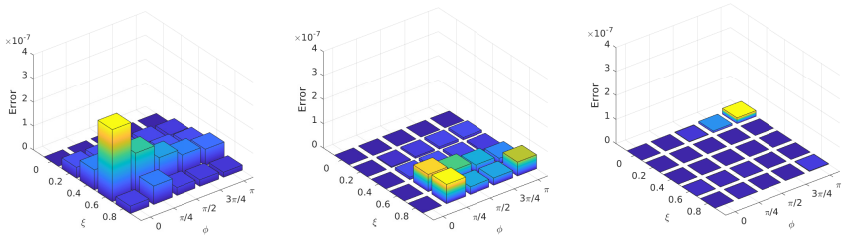

(a) $\boldsymbol{P^T P}$ **(b)** $\boldsymbol{P^T M}$ **(c)** $\mathcal{J}$

Figure A.2: Maximum of Error in preservation for varying ξ and ϕ using IM.

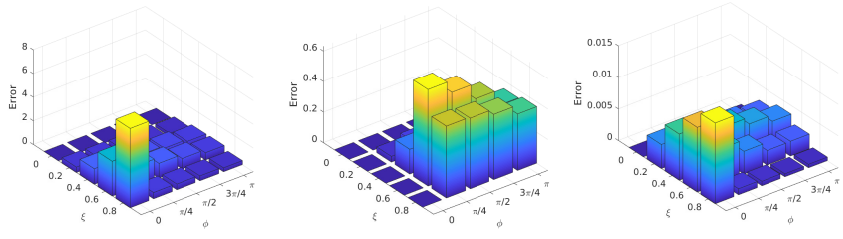

(a) $\boldsymbol{P^T P}$ **(b)** $\boldsymbol{P^T M}$ **(c)** $\mathcal{J}$

Figure A.3: Maximum of Error in preservation for varying ξ and ϕ using KM.

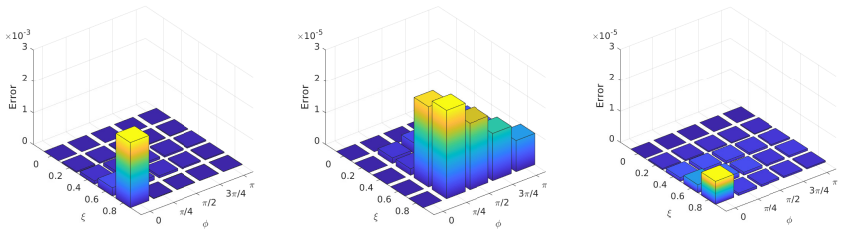

(a) $\boldsymbol{P^T P}$ **(b)** $\boldsymbol{P^T M}$ **(c)** $\mathcal{J}$

Figure A.4: Maximum of Error in preservation for varying ξ and ϕ using RK4.

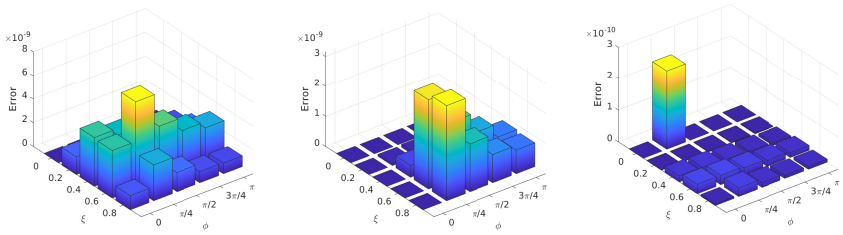

(a) $\boldsymbol{P}^T\boldsymbol{P}$ **(b)** $\boldsymbol{P}^T\boldsymbol{M}$ **(c)** $\mathcal{J}$

Figure A.5: Maximum of Error in preservation for varying ξ and ϕ using GL4.